# Unsteady Wake Rollup Modeling Using a Mollifier Based Filtering Technique

Gerasimos K. Politis

Professor, Department of Ship and Marine Hydrodynamics, School of Naval Architecture and Marine Engineering, National Technical University of Athens, Heroon Politechniou 9, Zografos, Athens, Greece

polit@central.ntua.gr

*Abstract*

3-D BEM formulations of unsteady lifting flow problems are paradigms of free boundary problems. The free boundary enters in the BEM formalism as the necessary spatial support of the velocity discontinuity, generated at the trailing edges of the lifting bodies. In the context of a BEM, this velocity discontinuity, alternatively termed a shear layer, is simulated by a surface dipole distribution or its equivalent singular vortex sheet. Free vortex sheets are inherently unstable and amenable to two well-known instabilities: the Kelvin-Helmholtz instability and the roll-up of their free edges. As a result, they show chaotic behavior with the passage of time. On the other hand, experimental evidence on flows around lift producing devices shows that the wake vorticity is organized in specific, problem dependent rollup patterns. In this paper we present a filtering technique, which by introducing artificial viscosity to our problem, suppresses the smaller scale instabilities, leaving the larger scale organized vortices to determine the rollup pattern of the free wake vorticity. Flow simulations are presented for a steadily advancing wing, a biomimetic wing at two different Strouhal numbers, a naval propeller at two different advance coefficients and a novel flexible oscillating duct propulsion device. The effect of the filtering parameters to the shear layer wake rollup pattern as well as to the calculated unsteady forces and moments is shown and discussed.

*Keywords*

*Unsteady Shear Layer Dynamics; Unsteady Wake Modeling; Lifting Flows around Flexible Bodies; Boundary Element Method*

## Introduction

Boundary element methods (BEM) have been long applied for the solution of flow problems around systems of streamlined lifting or non-lifting bodies. In the excellent book of Katz & Plotkin (2001) [10], almost all aspects and the state of the art of modern BEM formalisms, for fluid flow problems, are presented and discussed. BEM formulation of flow problems around lifting bodies is a paradigm of a 'free boundary problem'. The free boundary enters as the spatial support of the tangential velocity discontinuity, generated at the trailing edges of the wings. In the context of a BEM, this tangential velocity discontinuity is simulated by a dipole distribution or its equivalent singular vortex sheet. Typical remedies for the determination of this free boundary are: (a) the prescribed wake shape method or (equivalently) the frozen wake model by which the geometry of the free boundary is somehow a priori selected, (b) the wake relaxation method by which an initial supporting geometry is assumed and a corrector method based on Helmholtz vortex theorems is applied to obtain the final geometry, and (c) the time stepping algorithm by which the supporting geometry is derived by applying the free shear layer kinematic and dynamic boundary conditions in a step by step basis, Politis (2004) [18], Wu et al. (2006) [35]. Remedies (a) and (b) are applicable in either steady flow problems or in unsteady flow problems, where the unsteady flow field does not affect considerably the free shear layer position. Remedy (c) is more general and can be applied without limitations to the solution of any steady or unsteady flow problem. Unfortunately, application of remedy (c) requires coping with the inherent free singular vortex sheet instabilities. More specifically, it is well known that a singular vortex sheet is amenable to chaotic behavior due to a Kelvin-Helmholtz instability. Furthermore, the edge of the sheet induces infinite velocities to itself, fact which is related with the tip vortex rollup. Finally, a singular vortex sheet induces a non-physical tangential fluid velocity jump in its vicinity, not-existent in a viscous environment. An extensive discussion of the free vortex sheet instabilities, their chaotic behavior and corresponding simulation methods can be found in the review by Sarpkaya (1989)[26]. The same subject is discussed in the books by Saffman (1992) [25], Marchioro & Pulvirenti (1994)[12], Bajer & Moffatt (2004)[2] and Wu et al. (2006)[35]. Furthermore, a lot of experimental and theoretical/numerical works have been done on the subject, such as: Winckelmans & Leonard

(1993)[33], Ramsey (1996)[22], Riley & Lowson (1998)[23] in connection with delta wings, Wood & Grace (2000)[34], Krasny et al. (2002)[11] in connection with the vortex blob numerical simulation method, Dong et al. (2006)[9], Muijres & Lentink (2007)[14], Parker et al. (2007-2008)[16-17], Borazjani & Sotiropoulos (2008)[3], Wang et al. (2008)[32] and Bohl & Koochesfahani (2009)[4], to mention some of them.

Correct prediction of the dynamic evolution of the free shear layers is of high importance in many physical problems. For example, in biomimetic flows, the bird or fish wing performs large oscillatory (flapping) motions in comparison to its parallel translation, producing a highly deformed shear layer in the vicinity of the trailing edge, which affects the wing flow field. Similarly, in steady or unsteady naval propeller operation, the free shear layers are the main mechanisms of blade-to-blade interaction and introduction of the history effects. For higher loadings, the shear layers are limited in small regions behind the biomimetic wings or the propeller disk. As a result, a strong amalgamation of the free shear layers occurs and the problem of the mutual interaction of neighboring shear layers is superimposed to that of their self-action.

In Politis (2004) [18], we have formulate and solve the problem of flow around a propeller performing a general unsteady motion. A potential based BEM has been used to represent the propeller blades while a time stepping algorithm has been used to simulate free shear layer dynamics. During the period 2002-2008, this formulation, initially developed to treat propeller problems, has been expanded to include the simulation of any 3-D unsteady incompressible non-viscous flow problem around an arbitrary system of interacting non-lifting/lifting, rigid/flexible streamlined bodies. By flexible we mean pseudo-flexible; that is body deformation is determined by the user and not through coupling with the elastic behavior. The developed code has also been enriched with two new non-linear Kutta conditions of the pressure type, in addition to the initially used Morino type Kutta. The corresponding formulation is discussed in Politis (2009, 2011) [19-20] where comparisons with experimentally measured forces for biomimetic systems and propellers are also presented.

In this paper, we concentrate on the methodology used for the numerical determination of the free shear layer dynamics and more specifically, to the filtering technique, which suppresses the smaller scale instabilities leaving the larger scale dominant vortices to specify the dynamic evolution of the free shear layer surfaces. The method works successfully for any flow case, including that of large unsteady motions of interacting lifting rigid/flexible bodies. After a presentation of the method, we give a number of applications as follows: (a) a burst starting steadily advancing 3-D wing, (b) a biomimetic 3-D wing operating at two different Strouhal numbers, (c) a burst starting steadily advancing and rotating naval propeller operating at two different advance coefficients, and (d) a novel FOD (Flexible Oscillating Duct) propulsion system. The last application shows how our method can be used as a tool in analyzing and/or design of novel hydrodynamic systems based on the new Electro-active Polymer (EAP) materials, which can actively deform in a fluid environment, simulating the action of muscles, Cohen ed. (2004)[5]. In all cases, we show the effect of the filtering parameters to the obtained shear layer 3-D patterns. It is shown that for a range of the filtering parameters the free shear layers are organized in concrete 3-D space patterns, characteristic to the problem considered. We thus arrive at the notion of the 'attracting wake configuration' of a problem. Furthermore, calculated unsteady forces and moments are almost independent of the filtering parameters, even in chaotic shear layer pictures, as far as the shear layer geometry lies within the attracting configuration. Finally, it is shown that in certain flow problems, the old assumption of a frozen wake model results in unsteady forces and moments comparable to that using the more elaborate free wake model.

## Formulation

We start with a brief introduction of the main theoretical & numerical aspects of the BEM, necessary for the description of the filtering technique. A more detailed discussion can be found in Politis (2011) [20].

### Geometric Considerations

We build the geometry of complex systems of bodies using surface patches. Each patch consists of a number of bilinear quadrilateral elements. Two types of patches are allowed: (i) lifting patches and (ii) non-lifting patches. By combining patches we build lifting and/or non-lifting bodies. For the former case, the user has to determine the line

of flow separation in the surface of each lifting patch. The total system surface at time t is denoted by $SB(t)$. Total system Kutta strip surface at time t is denoted by $SK(t)$. Total system free shear layer surface at time t, excluding Kutta strips, is denoted by $SF(t)$, Politis (2011)[20].

*Velocity and Potential Representation Theorems*

We use an inertial (build in earth surface) frame of reference for the definition of velocities (body or fluid). A corresponding coordinate system (assumed Cartesian-orthogonal) is denoted by OXYZ.

As a result of the (known) unsteady motion of our system of bodies, in the region outer to $SB(t) \cup SK(t) \cup SF(t)$, a velocity (perturbation) potential $\phi$ exists which, at each time step, is expressible through its traces $\phi, \nabla \phi$ on the boundary points $Q \in SB(t) \cup SK(t) \cup SF(t)$.

Introduce:

$$F(P) = -\frac{1}{4\pi} \int_{SB(t)} \frac{\vec{n} \cdot \nabla \phi}{r} dS + \frac{1}{4\pi} \int_{SB(t)} \phi \frac{\vec{n} \cdot \vec{r}}{r^3} dS + \frac{1}{4\pi} \int_{SK(t)} \mu \frac{\vec{n} \cdot \vec{r}}{r^3} dS + \frac{1}{4\pi} \int_{SF(t)} \mu \frac{\vec{n} \cdot \vec{r}}{r^3} dS \qquad (1)$$

$$\vec{H}(P) = \frac{1}{4\pi} \int_{SB(t)} (\vec{n} \cdot \nabla \phi) \frac{\vec{r}}{r^3} dS + \frac{1}{4\pi} \int_{SB(t)} (\vec{n} \times \nabla \phi) \times \frac{\vec{r}}{r^3} dS + \frac{1}{4\pi} \int_{SK(t)} \vec{\gamma} \times \frac{\vec{r}}{r^3} dS + \frac{1}{4\pi} \int_{SF(t)} \vec{\gamma} \times \frac{\vec{r}}{r^3} dS - \frac{1}{4\pi} \int_{L'(t)} \mu \frac{d\vec{l} \times \vec{r}}{r^3} \qquad (2)$$

where: $P$ is the evaluation point (or control point) for either $F$ or $\vec{H}$, $\vec{n}$ is a unit normal vector at the boundary integration point $Q \in SB(t) \cup SK(t) \cup SF(t)$ showing inside the flow region, $\vec{r} = \vec{QP}$, $r = |\vec{QP}|$, $\mu$ is the dipole intensity with support on $SK(t) \cup SF(t)$ and $\vec{\gamma}$ the corresponding (to $\mu$) surface vorticity intensity given by:

$$\mu = \phi^+ - \phi^- \qquad (3)$$

$$\vec{\gamma} = \vec{n} \times \nabla \mu \qquad (4)$$

Finally, $L'(t)$ (integration region of the last line integral in the right hand side of equation (2)) is the free part of the line bounding the free shear layers, defined by: $L'(t) = \partial(SK(t) \cup SF(t)) - (SK(t) \cap SB(t))$.

With the aid of relations(1), (2) representation theorems for $\phi, \nabla \phi$ become:

$$\left.\begin{array}{l} \phi(P) = F(P) \\ \nabla \phi(P) = \vec{H}(P) \end{array}\right\} P \text{ outer to } (SB(t) \cup SK(t) \cup SF(t)) \qquad (5)$$

$$\left.\begin{array}{l} \phi(P) = \frac{1}{2}\phi(P) + F(P) \\ \nabla \phi(P) = \frac{1}{2}(\vec{n} \cdot \nabla \phi) \cdot \vec{n} + \frac{1}{2}(\vec{n} \times \nabla \phi) \times \vec{n} + \vec{H}(P) \end{array}\right\} \Leftrightarrow \left\{\begin{array}{l} \frac{1}{2}\phi(P) = F(P) \\ \frac{1}{2}\nabla \phi(P) = \vec{H}(P) \end{array}\right\} P \in SB(t) \qquad (6)$$

$$\left.\begin{array}{l} \phi^{+,-}(P) = \pm\frac{1}{2}\mu(P) + F(P) \\ \nabla \phi^{+,-}(P) = \pm\frac{1}{2}\vec{\gamma}(P) \times \vec{n}(P) + \vec{H}(P) \end{array}\right\} P \in SF^{+,-}(t) \qquad (7)$$

and similarly for $SK^{+,-}$. In relation (7), the superscripts $(^{+,-})$ denote the two sides of the free shear layer surfaces, while the unit normal $\vec{n}$ is directed from (-) to (+). Notice that some of the surface integrals for $F$ or $\vec{H}$ in relations (6) or (7) contain strong surface singularities of the Cauchy type. Thus, their meaning is realizable only in the principal value sense, Mikhlin (1965) [13].

*The Integral Equation*

Let $\vec{v}_A$ denotes the (known) velocity of the boundary point $A \in SB(t)$ and $\vec{n}$ a unit vector normal to body surface at $A$ with direction pointing into the flow region. Then, the no-entrance condition at $A$ has the form:

$$\nabla \phi \cdot \vec{n} = \vec{v}_A \cdot \vec{n} \tag{8}$$

Substituting (8) to the first of equations (6) and using (1) we get:

$$\frac{1}{2}\phi(P) - \frac{1}{4\pi}\int_{SB(t)}\phi\frac{\vec{n}\cdot\vec{r}}{r^3}dS - \frac{1}{4\pi}\int_{SK(t)}\mu\frac{\vec{n}\cdot\vec{r}}{r^3}dS = -\frac{1}{4\pi}\int_{SB(t)}\frac{\vec{n}\cdot\vec{v}_A}{r}dS + \frac{1}{4\pi}\int_{SF(t)}\mu\frac{\vec{n}\cdot\vec{r}}{r^3}dS, P \in SB(t) \tag{9}$$

This is a second kind Fredholm type Cauchy singular boundary integral equation for the determination of $\phi$ and $\mu$ on points of $SB(t)$ and $SK(t)$ respectively. In the right hand side of (9), the first term is a known integral (as far as the motion of the system of bodies is known). The second term is an integral over the free boundary $SF(t)$ known from the solution of the problem at previous time steps. The unknowns in the left hand side of (9) are the potential $\phi$ on $SB(t)$ and the dipole intensity $\mu$ on $SK(t)$. For their determination, the additional required condition is the Kutta condition at the separation lines (trailing edge in case of a wing flow w/o separation).

***The Kutta Condition***

Let the point $A \in SB(t)$. Let $\dfrac{d}{dt}\bigg|_A$ denote the time derivative for an observer built to the point A of the moving body and let $\vec{v}_A$ denote the known velocity of $A$. Then unsteady Bernoulli equation takes the form:

$$\frac{p - p_\infty}{\rho} = -\frac{d\phi}{dt}\bigg|_A - \frac{1}{2}\left(\nabla\phi - \vec{v}_A\right)^2 + \frac{1}{2}\vec{v}_A^2 \tag{10}$$

According to a pressure type Kutta condition, as we approach the trailing edge point from either pressure side (superscript +) or suction side (superscript -), the pressure should be continuous, i.e.: $p^+ = p^-$. Using(10), this becomes a quadratic (nonlinear) relation between $\phi^+, \nabla\phi^+, \phi^-, \nabla\phi^-$. Assuming steady linearized flow, Bernoulli equation degenerates to the famous Morino condition: $\mu_{\substack{\text{approaching L(t)}\\\text{from shear layer}}} = (\phi^+ - \phi^-)_{\substack{\text{approaching L(t)}\\\text{from body points}}}$ which is a linear equation in $\phi, \mu$. Either form of Kutta conditions can be handled by our code.

*Shear layer dynamics.* Kinematic and dynamic conditions on a free vortex sheet expressed in terms of the dipole intensity of the sheet result in the following equation, Politis (2004)[18], Wu et.al.(2006)[35]:

$$\frac{D\mu}{Dt} = 0 \tag{11}$$

where $D/Dt$ denotes a material derivative for $\mu$ based on the mean perturbation velocity $>\vec{v}<$ of the shear layer:

$$>\vec{v}<= \frac{\nabla\phi^+ + \nabla\phi^-}{2} = \vec{H}(P) \tag{12}$$

or in developed form:

$$>\vec{v}(P)<= \frac{1}{4\pi}\int_{SB(t)}(\vec{n}\cdot\nabla\phi)\frac{\vec{r}}{r^3}dS + \frac{1}{4\pi}\int_{SB(t)}(\vec{n}\times\nabla\phi)\times\frac{\vec{r}}{r^3}dS + \frac{1}{4\pi}\int_{SK(t)}\vec{\gamma}\times\frac{\vec{r}}{r^3}dS + \frac{1}{4\pi}\int_{SF(t)}\vec{\gamma}\times\frac{\vec{r}}{r^3}dS - \frac{1}{4\pi}\int_{L'(t)}\mu\frac{d\vec{l}\times\vec{r}}{r^3} \tag{13}$$

Equation (11) informs us that the dipole surface $SF(t)$, supporting the dipoles with intensity $\mu(\xi,\eta)$, is travelling with velocity $>\vec{v}<$, where $\xi, \eta$ denotes a set of curvilinear surface coordinates for the points on $SF(t)$. Thus, if a $\mu$ surface exists at time $t$, we can find its new position, at time $t + dt$, by deforming it by $>\vec{v}<\cdot dt$.

***Calculation of Forces, Moments and Power***

Let $\vec{F}(t)$ denote the total force exerted by the fluid to the body at $A \in SB(t)$. This force is a sum of pressure forces normal to the body (denoted by $\vec{P}(t)$) and viscous forces tangential to body (denoted by $\vec{D}(t)$). Thus: $\vec{F}(t) = \vec{P}(t) + \vec{D}(t)$. Pressure forces can be calculated from equation (10) while drag forces can be found assuming a

local at $A$ viscous drag coefficient. Assuming a reference point for moments $\vec{r}_M(t)$, the total instantaneous system force/moment can be calculated by the formulas:

$$\vec{F}_{system}(t) = \int\limits_{SB(t)} \vec{F}(t)dS, \vec{M}_{system}(t) = \int\limits_{SB(t)} \vec{r}_M(t) \times \vec{F}(t)dS \tag{14}$$

The last formulas can be applied to the whole system (use $SB(t)$ as integration region), or to one or more bodies of our configuration (use a subset of $SB(t)$ as integration region). In propulsion problems, there is always a preferable instantaneous direction in which the system moves. Let $\vec{V}(t)$ the instantaneous velocity of the system along this direction. Then the instantaneous useful power of the system is given by: $EHP(t) = \vec{V}(t) \cdot \vec{F}_{system}(t)$ ($EHP$: Effective Horse Power). The net instantaneous power interchange of our system with the environment is given by: $\int\limits_{SB(t)} \vec{F}(t) \cdot \vec{v}_A(t) \cdot dS$. Then the power provided to the system, termed DHP (Delivered Horse Power), is given by:

$$DHP(t) = \int\limits_{SB(t)} \vec{F}(t) \cdot \vec{v}_A(t) \cdot dS - EHP(t) \tag{15}$$

The ratio $EHP(t)/DHP(t)$ defines the instantaneous efficiency of our system. Notice that the previous formulas can be applied equally well to either rigid or flexible bodies.

### Discretization and Solution

Subdivide $SB(t)$ into $N_B$ elements. Subdivide $SK(t)$ into $N_K$ elements. Subdivide $SF(t)$ into $N_F$ elements. Four node quadrilateral elements have been used for the subdivision of body and shear layer boundaries. Assume piecewise constant $\phi$ and $\vec{n} \cdot \nabla \phi$ for all elements on $SB(t)$. Assume piecewise constant $\mu$ for all elements on $SK(t) \cup SF(t)$. Denote these constant values by $\phi_i, \sigma_i (=(n \cdot \nabla \phi)_i), \mu_i$ where the range of index (i) is adapted accordingly. With the aid of the previous assumptions/notation integral, equation (9) becomes:

$$\frac{1}{2}\phi_i - \sum_{j=1,N_B} B_{i,j}\phi_j - \sum_{j=1,N_K} B_{i,j}\mu_j = \sum_{j=1,N_B} A_{i,j}\sigma_j + \sum_{j=1,N_F} B_{i,j}\mu_j \tag{16}$$

$$A_{i,j} = -\frac{1}{4\pi}\int\limits_{E_j} \frac{dS}{|QP_i|}, B_{i,j} = \frac{1}{4\pi}\int\limits_{E_j} \frac{\vec{n}(Q) \cdot \overrightarrow{QP_i}dS}{|QP_i|^3} \tag{17}$$

and $E_j$ denotes the surface of the $j^{th}$ element from either $SB(t), SK(t), SF(t)$ and $P_i$ denotes the $i^{th}$ control point (centroid of $E_i$) on $SB(t)$. Relation (16) applied at the $N_B$ centroids of the body elements, gives $N_B$ linear equations for the determination of the $\phi_j, \mu_j$. The $N_K$ additional equations required for the calculation of $\mu_j$ are taken from the satisfaction of the Kutta condition on $SK(t) \cap SB(t)$ (i.e. trailing edges). In our code we implement three alternative forms of the Kutta condition: (i) The first alternative consists of a linear Morino condition, which in discretized form becomes: $\mu_i = \phi_{i^+} - \phi_{i^-}$ ($i^+$ and $i^-$ denote element numbers on body, neighboring to trailing edge from different sides and $i$ denotes element number on kutta strip, neighboring to the same point of the trailing edge), (ii) The second alternative consists of a nonlinear pressure type Kutta in the form of equation $p^+ = p^-$ with the additional conditions that the downstream length of the Kutta-Strip element is calculated according to the total velocity there and the kutta-strip element is either tangential to blade face or blade back according to the local value of circulation at this span-wise position, (iii) The third alternative consists of a 'mixed type Kutta' i.e. partly Morino and partly Pressure type. We have found that at higher loadings, a pressure type Kutta at blade tips is too strong and occasionally leads to a destruction of the shear layer geometry at those regions. Thus, we have decided to introduce a third alternative, the "mixed Kutta", i.e. a Morino condition at the tips of the separation line and a pressure type Kutta at all other points. If alternatives (ii) or (iii) have been selected, the resulting system of equations is nonlinear and it is solved by using a Newton iteration method, with starting value taken from a Morino type Kutta (first alternative).

With the previous discretization scheme in mind, the discretized formula for the calculation of $> \vec{v} <$ at points on $SF(t)$, needed for the application of the shear layer deformation scheme, becomes:

$$> \vec{v}_i <= \sum_{j=1,N_B} \vec{C}_{i,j}\sigma_j + \sum_{j=1,N_B} \vec{D}_{i,j}\phi_j + \sum_{j=1,N_k} \vec{D}_{i,j}\mu_j + \sum_{j=1,N_F} \vec{D}_{i,j}\mu_j \tag{18}$$

where:

$$\vec{C}_{i,j} = \frac{1}{4\pi}\int_{E_j} \frac{\overline{QP_i}\cdot dS}{\left|QP_i\right|^3}, \quad \vec{D}_{i,j} = \frac{1}{4\pi}\int_{\partial E_j} \frac{\vec{l}(Q)\times\overline{QP_i}\cdot dl}{\left|QP_i\right|^3} \quad (\vec{l} \text{ a unit tangent vector to } \partial E_j) \tag{19}$$

For the derivation of formula for $\vec{D}_{i,j}$ the equivalency of a constant dipole element with a line vortex at its boundary has been used, Politis (2004) [18]. Furthermore, for a bilinear boundary element $E_j$, its boundary $\partial E_j$ consists of four straight lines. Thus, the corresponding line integral in equation (19) can be calculated analytically. In detail: let $\partial E_j = AB \cup BC \cup CD \cup DA$ ( $A, B, C, D$ denote the nodes of element $E_j$ ). Then: $\vec{D}_{i,j} = \vec{D}_{i,j}\big|_{AB} + \vec{D}_{i,j}\big|_{BC} + \vec{D}_{i,j}\big|_{CD} + \vec{D}_{i,j}\big|_{DE}$. The contribution $\vec{D}_{i,j}\big|_{AB}$ to $\vec{D}_{i,j}$ from the side $AB$ (and similarly from sides: $BC, CD, DA$ ), to the control point $P$, is given by the relation:

$$\vec{D}_{i,j}\big|_{AB} = \frac{1}{4\pi h}(\cos\alpha + \cos\beta)\frac{\overline{PA}\times\overline{PB}}{\left|\overline{PA}\times\overline{PB}\right|} \tag{20}$$

where $\alpha = \measuredangle AB, AP$, $\beta = \measuredangle BA, BP$ and $h$ denotes the normal distance from control point $P$ to the line $AB$.

Solution of our problem is implemented by a time stepping algorithm as follows:

At each time step:

a. Find the next geometric position of the system of bodies.

b. Generate corresponding Kutta strips, for the case of lifting bodies, introducing thus the extra unknowns required for the Kutta condition satisfaction.

c. Solve the system consisting of the "no-entrance", equation(16), and "Kutta" conditions. In case of pressure type Kutta, a Newton iteration is used at this step.

d. Deform the free shear layers to their new positions, by applying a special filtering technique (to be discussed later) to calculate $> \vec{v} <$, equation(18).

e. Output results (pressures, forces, velocities, position of free shear layers) at this time step, in a form of TECPLOT compatible files.

f. Proceed to the next time step and repeat the calculation starting from step (a).

## The Filtering Technique

From the phenomenological point of view, the physical mechanisms of either the self-action of a free shear layer or the mutual interaction between neighboring shear layers, are mainly viscous and as such are excluded from the modeling capabilities of a rigorous BEM formulation based on the representation theorems for potential and velocity.

More specifically, determination of either the shear layer self-motion or its interaction with the neighboring shear layers requires evaluation of the velocity $> \vec{v} <$, equation(18), at control points $P \in SF(t)$. In our formulation we use as control points, the grid nodes of the moving grid representing the free shear layer at time $t$. Considering the terms in the right hand side of formula(18), we observe that only the last two contribute to $> \vec{v} <$ in a singular manner. This singular manner is explicitly expressed by relation (20). A heuristic proposal for the elimination of the singularity is offered by either the 'Lamb-Oseen' or the 'Burgers' vortices, which are special exact solutions of

the Navier-Stokes equations. In both cases, the azimuthal velocity $u_\theta$ of a vortex filament is given by the equation, Wu et al (2006) [35]:

$$u_\theta = \frac{\Gamma}{2\pi r}(1 - e^{-c \cdot \left(\frac{r}{R}\right)^p}), p = 2 \tag{21}$$

where: $\Gamma$ denotes the intensity of the vortex filament, $r$ the radial distance of the control point from the core of the filament, $c$ is a constant characterizing the range of action of the term $(1 - e^{-c \cdot \left(\frac{r}{R}\right)^p})$ and $R = 2\sqrt{\nu \cdot t}$ is a time dependent characteristic length used to make the action distance $r$ non-dimensional ($\nu$ denotes the kinematic viscosity of the fluid and $t$ the age of the vortex).

Comparing formula (21) with formula (20) applied to the case of an infinite singular vortex line ($\alpha = 0^0, \beta = 0^0 \Rightarrow \cos\alpha + \cos\beta = 2$), we observe that they are similar except for the multiplicative factor:

$$m(c, p, r/R) = (1 - e^{-c \cdot \left(\frac{r}{R}\right)^p}), p = 2 \tag{22}$$

which 'mollifies' the singularity at $r = 0$, substituting it by a viscous vortex core of finite diameter, controlled by the parameters: $c, p, R$. Rearranging the terms in (22) and taking the logarithms we get: $c = -\ln(1-m)/\left(\frac{r}{R}\right)^p$. Assuming a characteristic intensity $m = 0.5$ at $r/R = 1$, the mollifier constant $c$ can readily been calculated as: $c = -\ln(0.5) = 0.69314718$ independent of $p$. In this case, the mollifier function is uniquely defined by its radius $R$ and its power $p$ ($p = 2$ for vortex filaments).

Formula(21), for $\Gamma = 2\pi$ and preselected $c = 0.69314718, p = 2, R = 1$, is shown in figure 1. Formula (22) is shown in figure 2 for three different values of the parameter $p = 2, 3, 4$ and with $c = 0.69314718$.

Notice that mollifier functions have already been introduced in vortex particle flow simulation methods, Winckelmans & Leonard (1993) [33], Krasny et. al. (2002) [11].
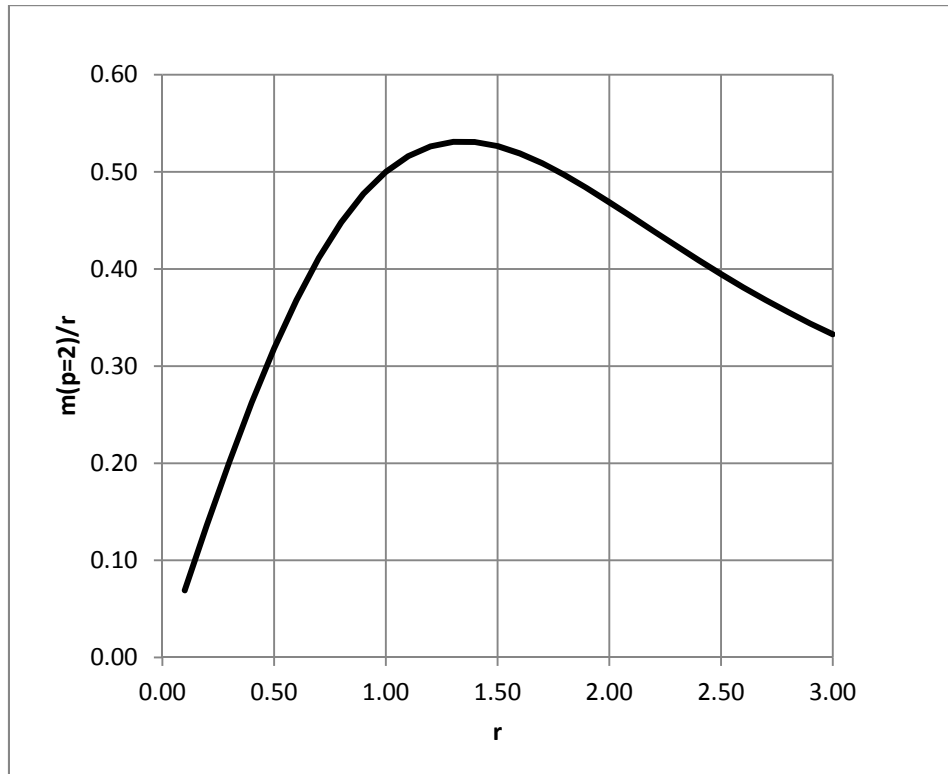


FIGURE 1. AZIMUTHAL VELOCITY OF A LAMB-OSEEN VORTEX. $\Gamma = 2\pi, c = 0.69314718, p = 2, R = 1$
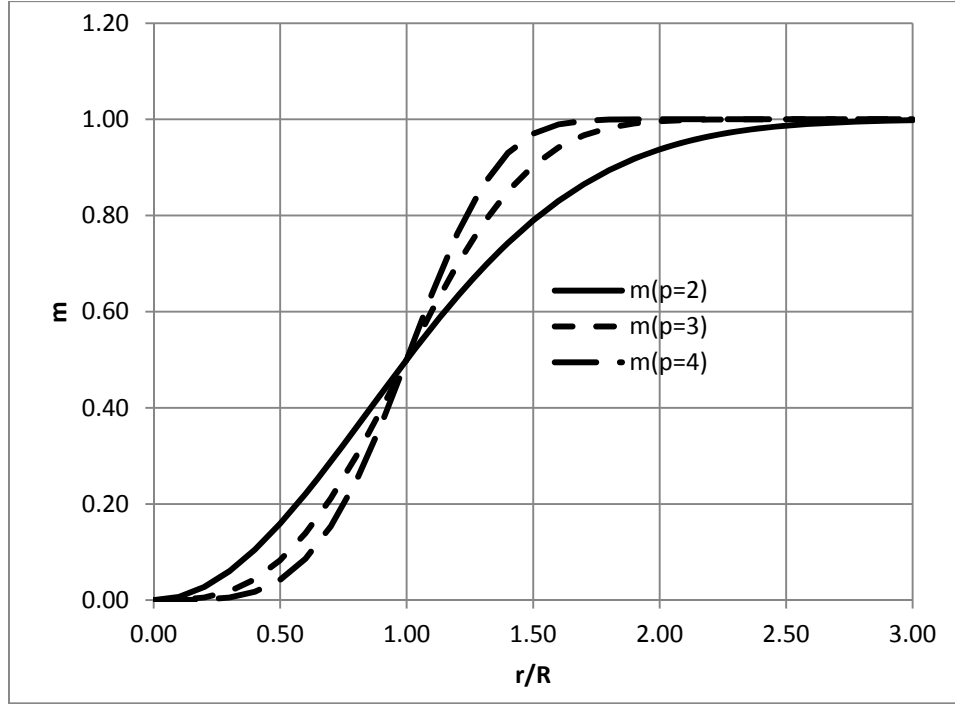
FIGURE 2. MOLLIFIER FUNCTION, $c = 0.69314718$, $p = 2, 3, 4$

With the aid of the mollifier function (22), formula (20) becomes:

$$\overline{\overline{\vec{D}_{i,j}}}\Big|_{AB} = (1 - e^{-c\left(\frac{h}{R}\right)^{p}})\frac{1}{4\pi h}(\cos\alpha + \cos\beta)\frac{\overline{PA}\times\overline{PB}}{\left|\overline{PA}\times\overline{PB}\right|}, p = 2 \qquad (23)$$

where $\overline{\overline{\vec{D}_{i,j}}}\Big|_{AB}$ denotes the mollified equivalent to $\vec{D}_{i,j}$. Considering formula (18) we observe that the $\vec{D}_{i,j}$ is met at the second, third and fourth terms in its right hand side. Since the control point for $> \vec{v}_i <$ belongs to $SF(t)$, only the third and fourth terms result in singular behavior and thus have to be mollified (i.e. use $\overline{\overline{\vec{D}_{i,j}}}\Big|_{AB}$ instead of $\vec{D}_{i,j}$). This observation is correct for all control points on $SF(t)$ with the exception of the region of $SF(t)$ in the vicinity of the Kutta strip (i.e. adjacent to the trailing edges). In this region, the induced velocity is strongly affected by both the free shear layer and the body elements. By applying a filtering process solely to the free shear layer dipole elements, an 'asymmetry' in the induced velocities in the vicinity of the Kutta strip can occur, which can trigger the breakdown of the shear layer geometry at those points. This danger is more pronounced at the first few time steps of a burst starting simulation, where a strong starting vortex is created in the vicinity of the trailing edges. To avoid the numerical instability, the second term in the right hand side of equation (18) (i.e. the induced velocity contribution from body potential) has to be mollified as well. Furthermore, for the same symmetry reasons, the mollifier function has to be smooth (or at least continues) in its extended support: $SB(t) \cup SK(t) \cup SF(t)$. In our formulation, we satisfy this condition by taking the body mollifier radius $R$ to be constant for all body elements with a value equal to the shear layer mollifier radius $R$ at the trailing edge region.

It is a well-known fact that viscous diffusion increases the diameter of the vortex core of a viscous vortex filament. This is the physical content of the relation $R = 2\sqrt{\nu \cdot t}$ introduced previously. Thus, older vortices have larger viscous diameters (or action ranges). According to the time stepping algorithm, a new span-wise strip of ring vortices is added to each shear layer at each time step. Thus, different span-wise vortex strips have different ages. In our formulation, we take heuristically this effect into consideration, by introducing age dependent mollifier radii $R$. This plays a crucial role in delaying the onset of chaos in the older parts of the free shear layers, especially in cases with higher hydrodynamic loadings. A measure of the age of a span-wise strip can be provided by the number of strips in-between this strip and the trailing edge. From the experience gained from the practical applications of the method, we know that proper values for $R$ are: 0.5% to 15% of the diameter of the convex hull

(denoted by $D_{CH}$ ), containing our system of bodies, depending from the hydrodynamic loading, the body geometric details and the motion details of our system.

In the case of a close contact of the freely moving shear layer with a body surface (for example in a kaplan type ducted propeller, the blade shear layers pass very close to the duct surface) numerical instabilities may occur due to the zeroing of the denominator in the respective formulas for the calculation of velocities and/or potentials, equations (18) and (16), which can lead to an intrusion of the shear layer inside the body. To avoid such an instance, the developed code contains an algorithm by which user controlled 'elastic shields' are applied to the bodies, avoiding thus the intrusion of a shear layer node inside the body. This shield methodology is planned to be discussed in a future paper.

## Applications

### *The Shear Layer Geometry of a Burst (Step) Starting Wing*

The first application concerns the flow around a burst starting wing. The wing has a span $s = 2m$ , a chord at mid-span $c = 1m$ and a chord at tip $c_{tip} = 0.3m$ . The wing has an X-skewback of 30 degrees, measured at the $c/3$ span-wise line from the leading edge. A NACA 0012 section has been used. Calculations have been performed for an advance velocity $V = 5m/s$ at an angle of attack $a = 20^0$ , using a blade grid with 40 span-wise elements and 16 chord-wise elements for either face or back. We use an equally spaced span-wise and a cosine spaced chord-wise subdivision. Total simulation time is $1.0s$ subdivided in 84 time steps, with each time step equal to $\delta t = 0.0119s$ . The previous selections result in an X-extension of the free shear layer, approximately equal to 5 chord lengths. Furthermore, $D_{CH} = 2m$ for this example. A mixed type Kutta condition has been used in this simulation and all other simulations except the last (FOD), in which a pressure type Kutta has been used.

Simulations have been performed for the following wake models (WM): (a) a free WM with mollifier radius $R/D_{CH} = 0.005$ , (b) a free WM with mollifier radius $R/D_{CH} = 0.07$ , (c) a free WM using a time dependent mollifier radius $R(t)$ , and (d) a frozen WM.  In case (c) the mollifier radius varies linearly between time steps, with the following break points ( *its* denotes the order of the shear layer span-wise strip with regard to the trailing edge): $(its, R(t)/D_{CH}) = (1, 0.005), (21, 0.03), (84, 0.1)$ . In case (d), the support of the free shear layer dipoles coincides with the trace in time of the trailing edge (i.e. located at the undistorted flow position).

Figure 3 shows the free shear layer geometry for WM (a) colored with the dipole intensity $\mu$ . Since $\vec{\gamma} = \vec{n} \times \nabla \mu$ , equation (4), the constant- $\mu$ lines, shown in the figure (and all similar figures to follow), are tangent to the surface vorticity intensity vector $\vec{\gamma}$ . Thus, figure 3 represents a characteristic quadrilateral ring vortex with three free sides, consisting of the two tip vortices and the starting vortex, and a bound side coinciding with the wing body. As we move downstream from the wing trailing edge, the tip vortex roll-up gradually develops, while approaching the junction point with the starting vortex instabilities appear. By increasing the mollifier radius to $R/D_{CH} = 0.07$ , WM(b), the tip vortex instability is suppressed but with a similar effect to the tip vortex roll-up, figure 4.  To allow a simultaneous development of the tip vortex roll-up with a suppression of the starting vortex instability, a time dependent filter can be used. Corresponding results are shown in figure 5. With the time dependent filter, WM(c), the starting vortex instability has successfully been limited, without affecting the tip vortex rollup at the region near the wing trailing edges.

Comparing the 3-D views shown on figures 3, 4 and 5, we conclude that irrespective of the selected filters, a definite shear layer 3-D pattern exists in the form of a 3-D ring vortex. A better sense of the effect of the filters to the shear layer pattern can be obtained, if we compare the slices of the shear layers with a plane normal to the X axis for different mollifier radii. Figure 6 shows such a comparison for the plane normal to the X-axis at the point $x = -2m$ (with regard to the global inertia coordinate system). Solid line refers to WM (a), dashed line refers to WM (b) and dashed-dot line to WM(c).

Attempts to simulate the shear layer geometry of a steadily advancing wing, using singular vortex sheets, has been made in the past by other researchers with results similar to that presented here. We refer to the works of Ramsey (1996) [22] and Wood & Grace (2000)[34].

Figure 7 presents comparisons of the vertical (along Y-axis) force, divided by fluid density $\rho$, obtained using either of WM (a), (b), (c) or (d). The curves in figure 7 are labeled as follows: WM (a): 0.005, WM (b): 0.07, WM(c): $R(t)$, WM(d): *frozen*. The results for the vertical force are practically the same for WM's: (a), (b) and (c). Those predictions differ from the corresponding frozen wake model by about $0.6\%$. Thus, a frozen or a generalized wake model can be an attractive alternative to the more elaborate free wake model, for predicting forces in a steadily advancing wing. This explains the success of the traditional lifting line or lifting surface theories in predicting the steady lift for wings using either a frozen or a generalized wake model.
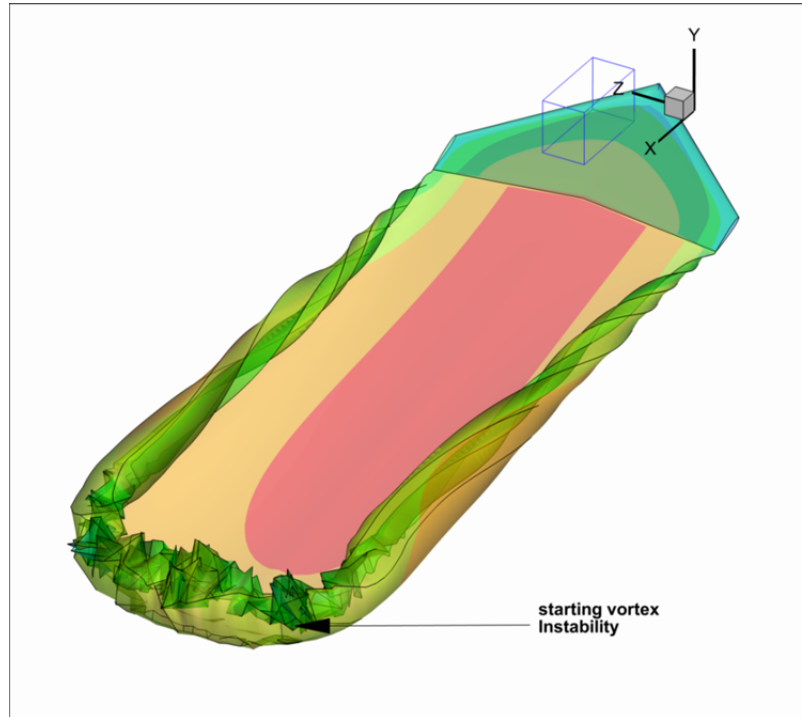


FIGURE 3. FREE SHEAR LAYER OF A BURST STARTING WING FOR WM (A). WING COLORED WITH POTENTIAL INTENSITY. SHEAR LAYER COLORED WITH DIPOLE INTENSITY.
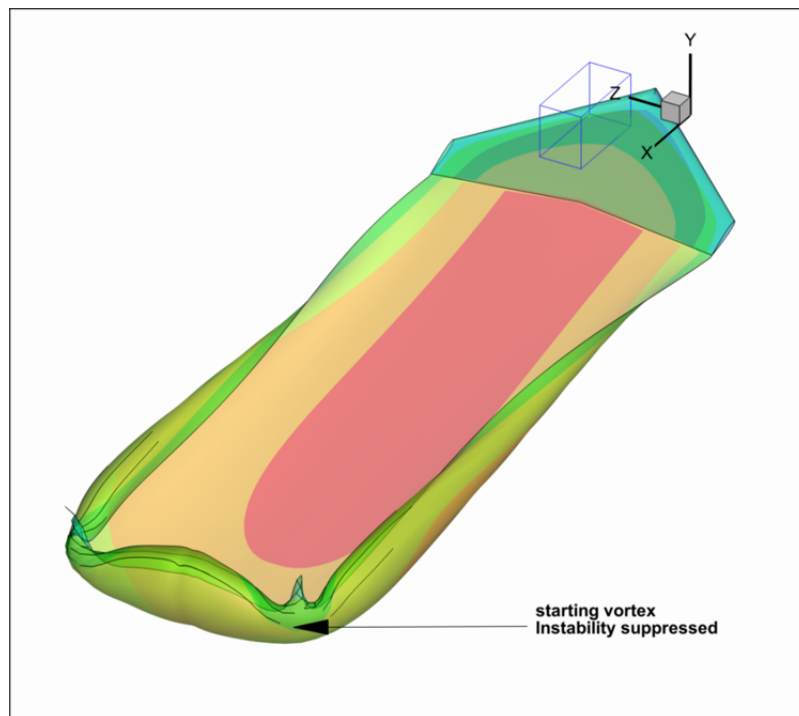


FIGURE 4. FREE SHEAR LAYER OF A BURST STARTING WING FOR WM (B).
TIP VORTEX ROLL-UP PARTIALLY SUPPRESSED. STARTING VORTEX INSTABILITY SUPPRESSED.
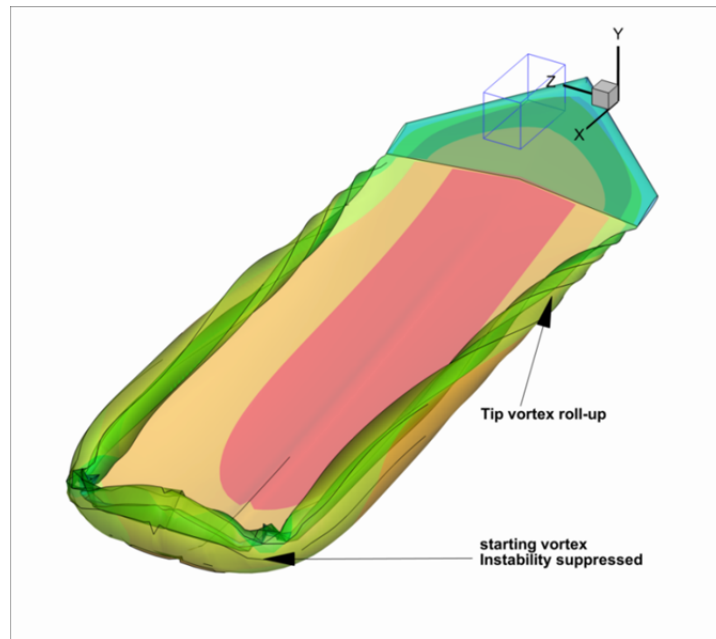
FIGURE 5. FREE SHEAR LAYER OF A BURST STARTING WING FOR WM (C).
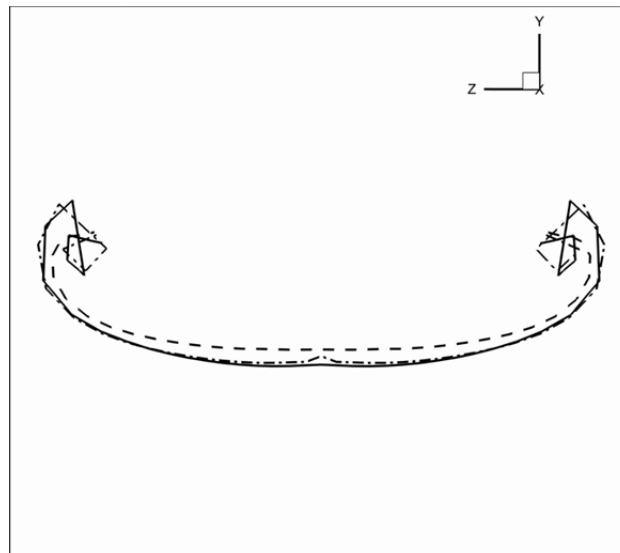


FIGURE 6. SLICE OF THE FREE SHEAR LAYER AT $x = -2m$ .SOLID LINE: WM(A), DASHED LINE: WM(B), DASHED-DOT LINE: WM(C)
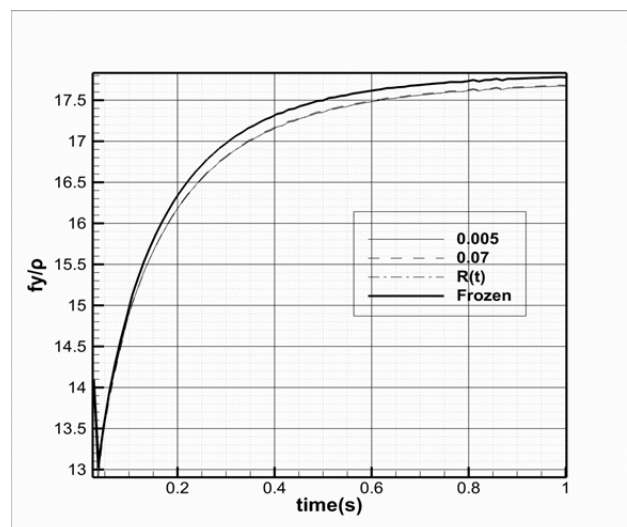


FIGURE 7. VERTICAL FORCE OF A BURST STARTING WING. PREDICTIONS WITH DIFFERENT WM'S

*The Shear Layer Geometry of a Biomimetic Wing*

Biomimetic wings are the subject of extensive investigations, since they are ideally suited in converting environmental (atmospheric or sea wave) flow energy to useful thrust, succeeding thus propulsive efficiencies well over one. An extensive collection of research works in the area can be found in the book of Taylor et al. (Eds.) (2010) [30]. The subject of aerodynamics of natural flyers is discussed in a recent book by Shyy et al. (2008) [27]. Reviews on the subject can be found in the papers of Triantafyllou et al. (2000) [31] and Rozhdestvensky & Ryzhov (2003) [24]. Experimental and numerical simulations of various biomimetic flow problems can be found in: Dong et al. (2006)[9], Muijres & Lentink (2007)[14], Parker et al. (2007-2008)[16-17], Wang et al. (2008)[32], Borazjani & Sotiropoulos (2008)[3], Bohl & Koochesfahani (2009)[4], Andro & Jacquin (2009)[1], to mention some of the most recent works on the subject.

Due to the obvious importance of biomimetic flow problems, we have selected it as our next application in a biomimetic wing. In the study of natural flyers and swimmers in cruising condition, it is found that the Strouhal number (which can be considered as a measure of their hydrodynamic loading), defined by:

$$St = \frac{2 \cdot f \cdot h_0}{V} \tag{24}$$

is within the range $0.2 < St < 0.4$, Triantafyllou et al. (2000)[31], Rozhdestvensky & Ryzhov (2003)[24], Taylor et al. (2003)[29]. In relation (24), $f$ denotes the common frequency of heaving or pitching, $h_0$ denotes a characteristic heave amplitude and $V$ the advance velocity. On the other hand, man-made biomimetic wings can be designed to operate in much higher hydrodynamic loadings (or Strouhal numbers). For those reasons, we have decided to present flow simulations at two different Strouhal numbers: $St = 0.5$ and $St = 1.0$. In both simulations, all data have been kept constant except frequency $f$ which has been doubled for the second case.

*Case with $St = 0.5$*

The selected wing geometry and BEM discretization is the same as that used in the previous example of a burst starting wing. The biomimetic wing advances with a velocity $V = 5.0 m/s$, performs a heaving oscillation with amplitude $h_0 = 0.5m$, a pitching oscillation with amplitude $25.0 \deg$ and a phase angle of $90.0 \deg$ (with respect to heaving) and a common (for both heave and pitch oscillations) frequency $f = 2.5 rps$. The pitching axis has been selected at 33% from the leading edge at mid-span. The total simulation time is $0.8s$ or two periods. 60 time steps have been used per period or 120 time steps total. The previous data resulted in a Strouhal number: $St = 0.5$.

Figure 8 shows the free shear layer geometry for a mollifier radius $R/D_{CH} = 0.01$ (where $D_{CH} = 2m$ as previously), colored with the surface dipole intensity $\mu$. An extensive instability of the shear layer is observed: (a) at its edges, and (b) at its span-wise strips which correspond to a sign change of the sectional angle of attack (defined with respect to the total undisturbed fluid velocity). By increasing the mollifier radius to $R/D_{CH} = 0.07$, the instability is suppressed in the major part of the free shear layer in figure 9. From figures 8 and 9, we observe that irrespective of the filter used, the shear layers occupy a certain region of the 3-D space with a well-recognized pattern. For a better confirmation of this conclusion, we compare the slices of the shear layers with planes normal to either the X or the Z axis in figures 10 and 11. Deformation of the shear layers can be used as a visualizer of the large scale vortices created by the motion of a biomimetic wing. Using this deformation, we conclude that the wake of a biomimetic wing consists of a train of oblique vortex rings which produce a repeated S-shaped 3-D wake pattern (reverse Karman Vortex Street). We can arrive at the same conclusion if we use the constant dipole intensity lines (used to color the shear layers) in figures 8 and 9, to visualize the surface vortex lines. This S-shaped attracting configuration in figure 10 is characteristic for all thrust producing biomimetic wings and has been experimentally observed by many authors, Triantafyllou et al. (2000)[31], Muijres & Lentink (2007)[14], Parker et al. (2007-2008)[16-17], Zhang & Zheng (2009)[36].

Figures 12 and 13 present comparisons of the unsteady biomimetic wing forces obtained using a free WM with that obtained with a frozen WM. For the free WM, the following mollifier radii have been used: $R/D_{CH} = 0.01$, $R/D_{CH} = 0.07$. Curve labeling follows that introduced in the example of a burst starting wing. It is shown that the

free WM results in practically the same X- and Y- forces, irrespective of the selected $R / D_{CH}$. Those forces differ from that obtained using a frozen WM only slightly. For example, at $t = 0.62s$, which is near the $fx / \rho, fy / \rho$ maximum values, the difference between the frozen wake and the free wake thrust force $fx / \rho$ is less than $1\%$. The corresponding difference for $fy / \rho$ is $2 - 3\%$. Notice finally that according to our sign conventions, the thrust force in figure 12 is negative. This is a result of the motion of the wing which has been selected in the negative direction (with respect to the inertia coordinate system $XYZ$ and to the fact that we have define positive 'forces' as that exerted to the body by the surrounding fluid).
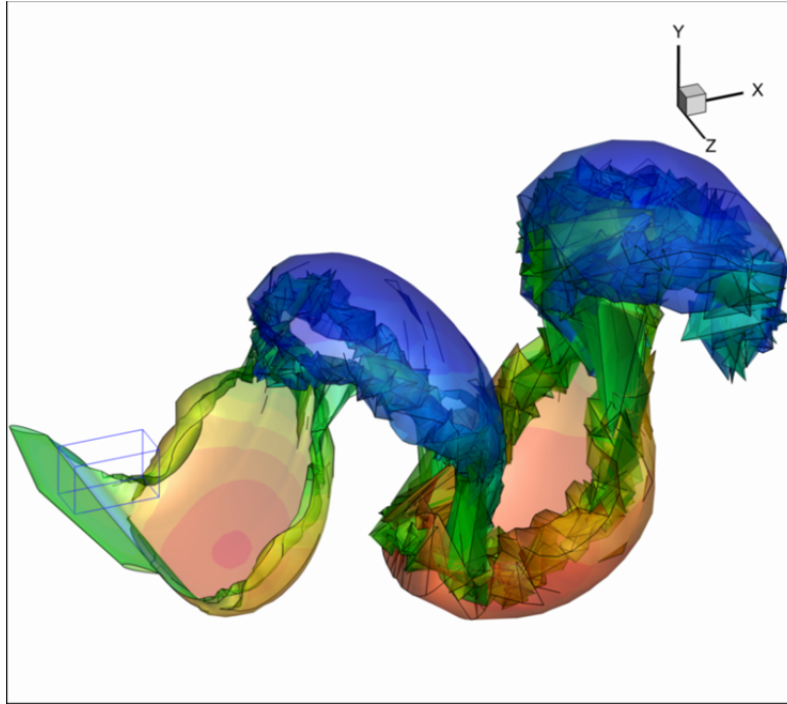


FIGURE 8. FREE SHEAR LAYER OF A BIOMIMETIC WING AT $t = 0.8s$ WITH EXTENSIVE VORTEX INSTABILITIES. WING COLORED WITH POTENTIAL INTENSITY. SHEAR LAYER COLORED WITH DIPOLE INTENSITY. $St = 0.5, R / D_{CH} = 0.01$
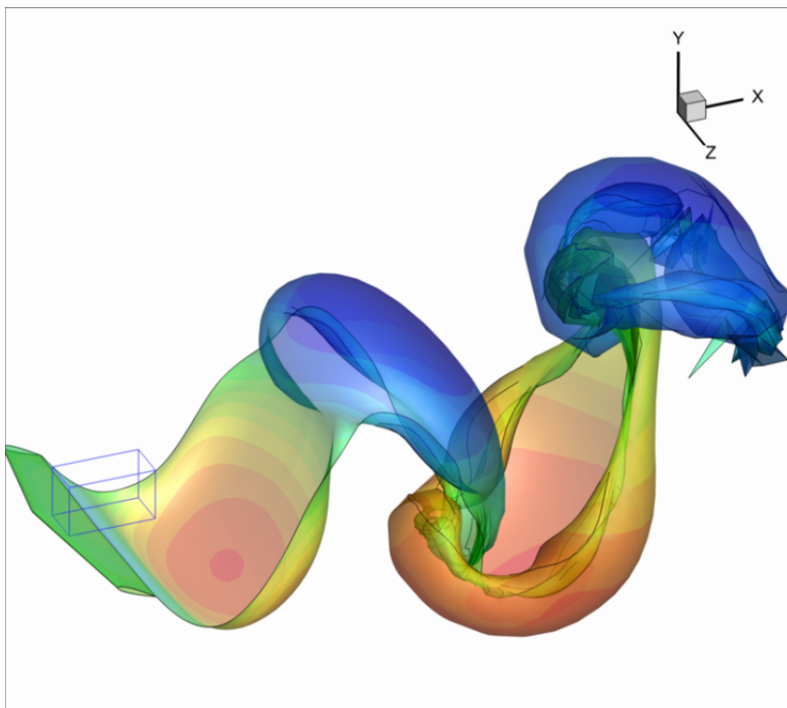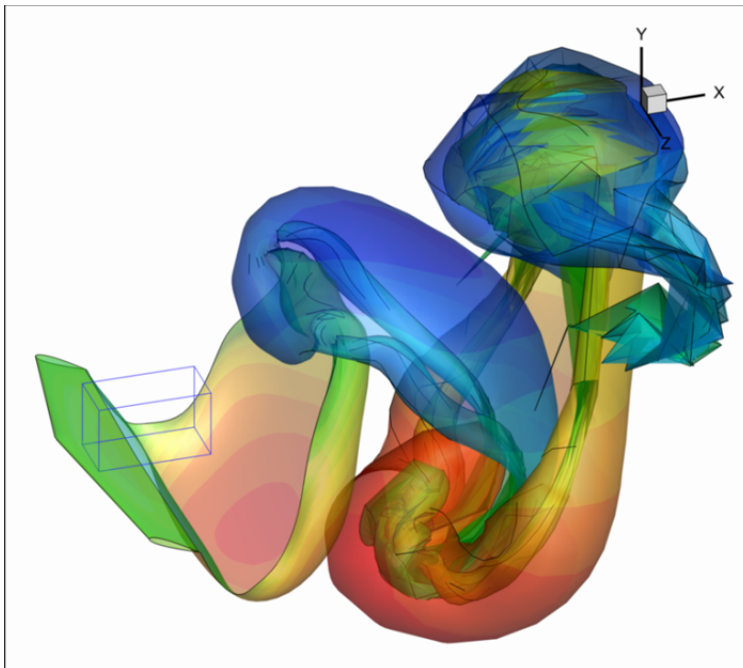


FIGURE 9. FREE SHEAR LAYER OF A BIOMIMETIC WING AT $t = 0.8s$ WITH INSTABILITIES SUPPRESSED IN THE MAJOR PART OF THE FREE SHEAR LAYER. $St = 0.5, R / D_{CH} = 0.07$
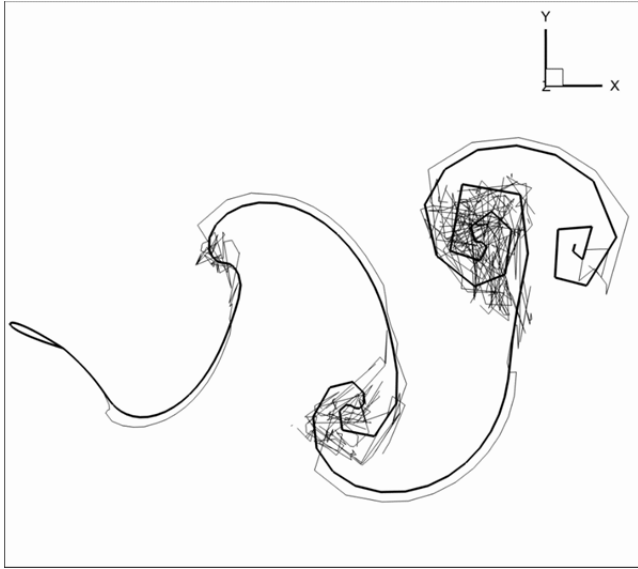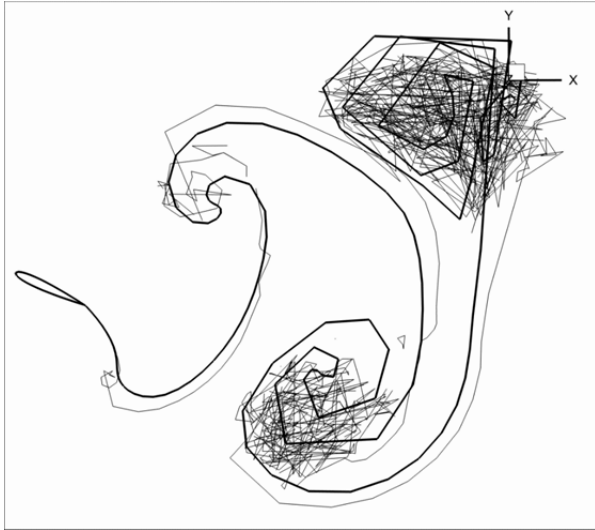
FIGURE 10. SLICE OF THE FREE SHEAR LAYER AT $t = 0.8s, z = 0.0m$ . REVERSE KARMAN VORTEX STREET WAKE PATTERN. HAIR LINE: $R / D_{CH} = 0.01$ , BOLD LINE: $R / D_{CH} = 0.07$
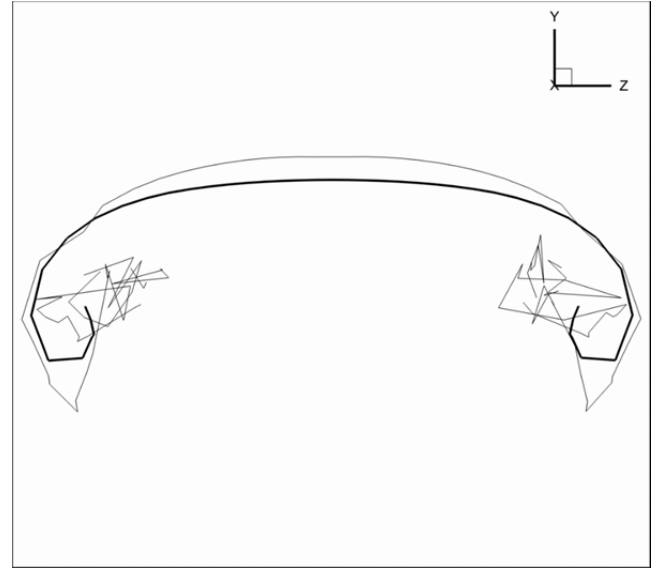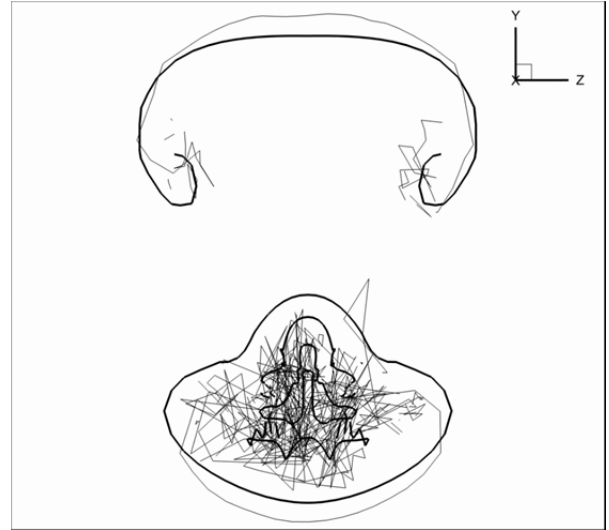


FIGURE 11. SLICE OF THE FREE SHEAR LAYER AT $t = 0.8s, x = -1.8m$ .HAIR LINE: $R / D_{CH} = 0.01$ , BOLD LINE: $R / D_{CH} = 0.07$
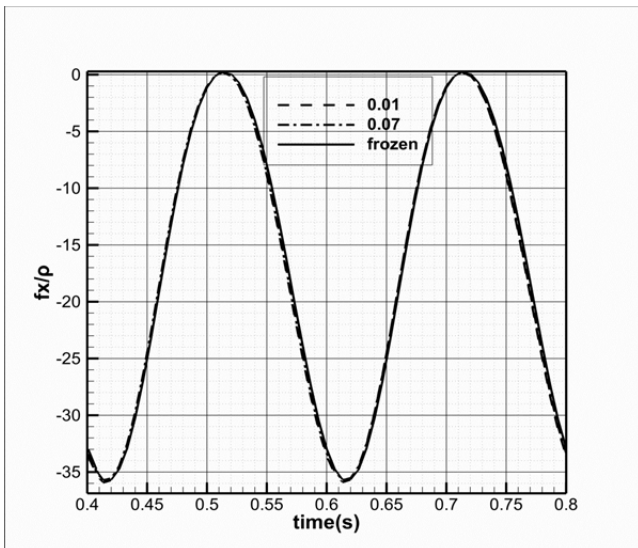


FIGURE 12. THRUST (X-AXIS) FORCE OF THE BIOMIMETIC WING – PREDICTIONS WITH DIFFERENT WAKE MODELS.
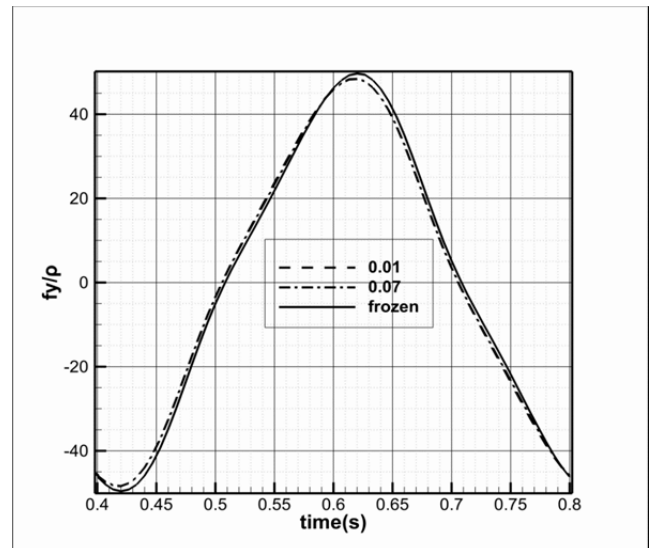


FIGURE 13. VERTICAL (Y-AXIS) FORCE OF THE BIOMIMETIC WING – PREDICTIONS WITH DIFFERENT WAKE MODELS

*Case with* $St = 1.0$

This example is similar to the previous one, except frequency, which has been doubled i.e. $f = 5.0 rps$ . The total simulation time for this case is $0.4s$ or two periods. 60 time steps have been used per period or 120 time steps total.

Figure 14 shows the free shear layer geometry for a mollifier radius $R / D_{CH} = 0.01$. We observe that the instabilities shown for the lower Strouhal in figure 8 have been strengthened. By changing the mollifier radius to $R / D_{CH} = 0.07$, the instability is again eliminated in the major part of the free shear layer in figure 15. From figures 14 and 15, we (again) observe that, irrespective of the filter used, the shear layers show a well-recognized pattern. This pattern is also shown in the slices of the shear layers with the planes normal to either the X or the Z axis in figures 16 and 17. Using the deformation of the shear layers to visualize the large scale vortices, we arrive (again) to the repeated-S shaped wake pattern or reverse Karman Vortex Street. Comparing figure 9 with figure 15, we observe that by increasing the Strouhal number (and consequently the hydrodynamic loading) the train of the oblique vortex rings has been limited to a region closer to the wing body.

Figures 18 and 19 present comparisons of the unsteady biomimetic wing forces obtained using a free WM with either $R/D_{CH} = 0.01$ or $R/D_{CH} = 0.07$, with that obtained with a frozen WM. It is shown that the free WM results in practically the same X- and Y- forces, irrespective of the selected $R/D_{CH}$. Those forces differ from that obtained using a frozen WM. For example, at $t = 0.32s$, which is near the $fx/\rho, fy/\rho$ maximum values, the difference between the frozen wake and the free wake thrust force $fx/\rho$ is $6-7\%$. The corresponding difference for $fy/\rho$ is $19-20\%$. Thus, by increasing the Strouhal number (equivalently the hydrodynamic loading), the differences between the frozen wake and the free wake become more pronounced. This is an expected consequence of the shear layer limitation in a region closer to the body surface as the Strouhal increases. Since birds and fishes operate at: $0.2 < St < 0.4$, it seems that the simpler frozen WM can be used in force predictions instead of the more elaborate free WM.
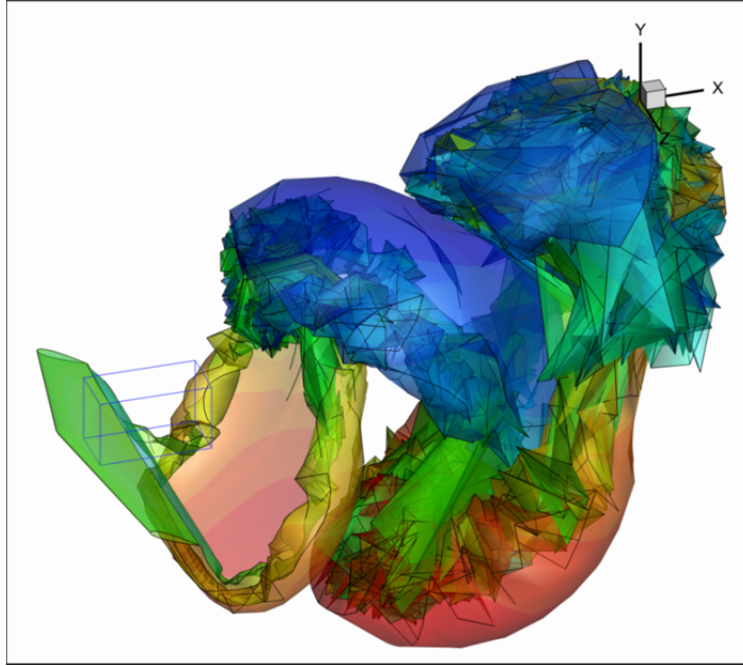


FIGURE 14. FREE SHEAR LAYER OF A BIOMIMETIC WING AT $t = 0.4s$ WITH EXTENSIVE VORTEX INSTABILITIES. $St = 1.0, R/D_{CH} = 0.01$



FIGURE 15. FREE SHEAR LAYER OF A BIOMIMETIC WING AT $t = 0.4s$ WITH INSTABILITIES SUPPRESSED IN THE MAJOR PART OF THE FREE SHEAR LAYER. $St = 1.0, R/D_{CH} = 0.07$

FIGURE 16. SLICE OF THE FREE SHEAR LAYER AT $t = 0.4s, z = 0.0m$ . REVERSE KARMAN VORTEX STREET WAKE PATTERN. HAIR LINE: $R / D_{CH} = 0.01$ , BOLD LINE: $R / D_{CH} = 0.07$ .



FIGURE 17. SLICE OF THE FREE SHEAR LAYER AT $t = 0.4s, x = -0.21m$ HAIR LINE: $R / D_{CH} = 0.01$ , BOLD LINE: $R / D_{CH} = 0.07$
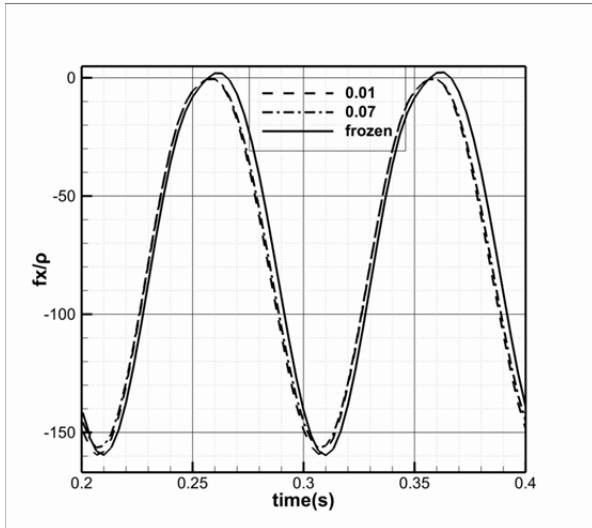


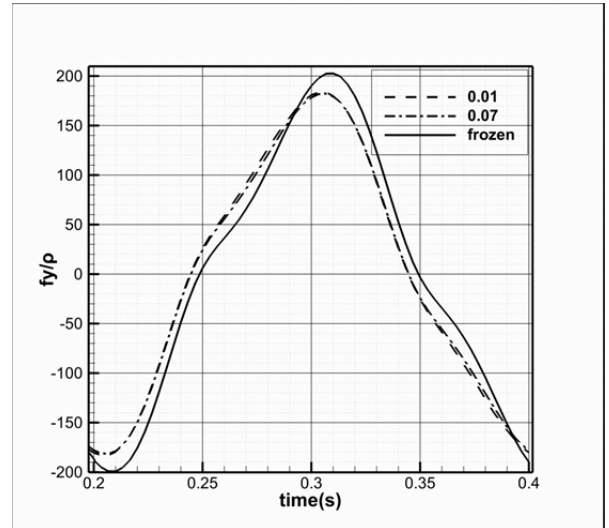FIGURE 18. THRUST (X-AXIS) FORCE OF THE BIOMIMETIC WING – PREDICTIONS WITH DIFFERENT WAKE MODELS.



FIGURE 19. VERTICAL (Y-AXIS) FORCE OF THE BIOMIMETIC WING – PREDICTIONS WITH DIFFERENT WAKE MODELS.

### The Shear Layer Geometry of a Burst Starting Naval Propeller

Our next application concerns estimation of the steady performance of burst starting naval propeller. The propeller is 3-bladed with a diameter $D = 5.7m$ , a pitch ratio $P/D = 1.1$ , a blade area ratio $A_E / A_0 = 0.55$ and its detailed characteristics are similar to those of a B-series propeller, Oosterveld & Oossannen (1975)[15], but with slightly increased tip-skew. Calculations have been performed using a blade grid of 24 radial elements and 16 chord-wise elements for either face or back. Propeller hub is included in our BEM modeling.

Calculations are performed at two propeller advance coefficients: $J = \dfrac{V}{f \cdot D} = 0.2$ and $J = 0.7$ . The first concerns operation at a heavily loaded point, while the second at a point with a lighter load, closer to propeller design point.

### Case with $J = 0.2$

The propeller moves with a velocity of advance $V = 2.28m / s$ and rotates with a frequency $f = 2rps$ or $120rpm$ . Flow simulation lasts for two full propeller revolutions with a propeller angular step of 6 degrees. This results in a total simulation time of $1.0s$ and 60 time steps per propeller turn or 120 time steps total.

In our first simulation, we have selected a mollifier radius $R/D_{CH} = 0.01$ where $D_{CH} = 5.7m$. Unfortunately, the execution of the computer code for this case has automatically been interrupted at $t = 0.21s$, with the error message: 'a highly deformed element has been detected'. This message has to do with a failure of the adaptive quadrature over an element and with the limits (accuracy and maximum number of integration points) set by the user of the code. Figure 20 shows the free shear layer geometry at time $t = 0.21s$, which corresponds to the last instance before the automatic code interruption. An extensive instability of the shear layer geometry is observed at the junction of the starting vortex with the hub vortex, which explains the automatic code interruption with the corresponding error message. By increasing the mollifier radius to $R/D_{CH} = 0.05$, the instability is suppressed allowing thus the finishing of the simulation. Figures 21 and 22 show the 3-D and YZ projected views of the free shear layer when $R/D_{CH} = 0.05$. From the transparent views, it is shown that at the rear downstream part of the free wake some instability still occurs. By further increasing the mollifier radius to $R/D_{CH} = 0.1$, the free wake instability is almost fully eliminated in figures 23 and 24. From figures 21 to 24, we observe that, irrespective of the filter used, the shear layers always occupy a certain region of the 3-D space with a well-recognized pattern similar to the shape of a 'mushroom'. Figures 25 and 26 compare slices of the shear layers with planes, which either contain the X axis or are normal to it. Using the deformation of the shear layers as a visualizer of the large scale vortices created by the propeller, we conclude that the wake of a propeller evolves as a result of a redistribution of both the starting and the tip vortices. The starting vortices are mainly responsible for the creation of angular momentum in the propeller race, while the tip vortices are connected with the creation of an axial momentum. With the passage of time the strong tip vortices, interact with the starting vortices, increasing their diameters and producing a 'mushroom' type downstream wake pattern. This mushroom vorticity pattern strengthens with time, accelerating the flow in the propeller disk and contracting the flow downstream the propeller disk. Our numerical findings are experimentally confirmed in the work of Stettler (2004) [28].

Figure 27 presents comparisons of the burst starting propeller thrust forces obtained using either a free WM or a frozen WM with experimental results. For the free WM, the following mollifier radii have been used:

$$R/D_{CH} = 0.01, \ 0.03, \ 0.05, \ 0.07, \ 0.10$$

Curve labeling follows that introduced in the example of a burst starting wing. It is shown that with the exception of an initial transient period, the free WM results in practically the same thrust force, irrespective of the selected $R/D_{CH}$. This force is very near to the experimental measurements, Oosterveld & Oossannen (1975) [15]. On the other hand, very large differences exist with the predictions obtained using a frozen WM. At the end of the simulation, those differences are of the order of 30% with a trend to increase with the passage of time in figure 27.
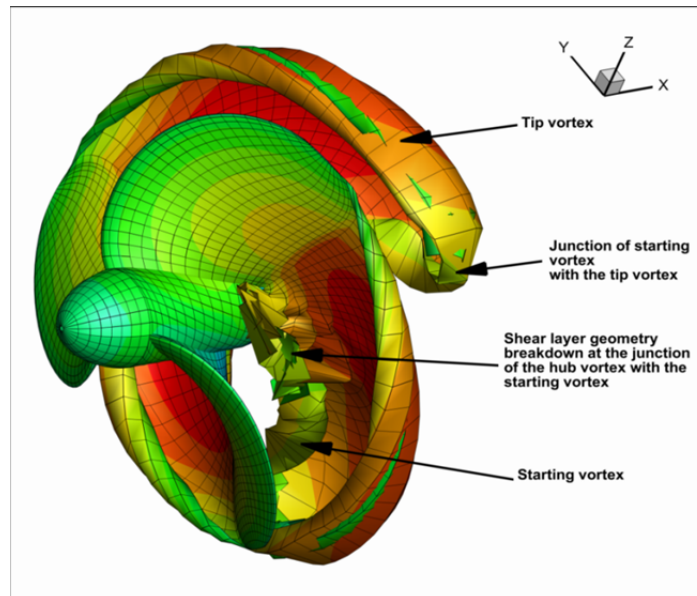


FIGURE 20. FREE SHEAR LAYER OF A PROPELLER AT $t = 0.21s$. EXTENDED SHEAR LAYER INSTABILITIES OCCUR AT THE JUNCTION OF THE HUB VORTEX WITH THE STARTING VORTEX. BLADES COLORED WITH POTENTIAL INTENSITY. SHEAR LAYERS COLORED WITH DIPOLE INTENSITY. $J = 0.2, R/D_{CH} = 0.01$.
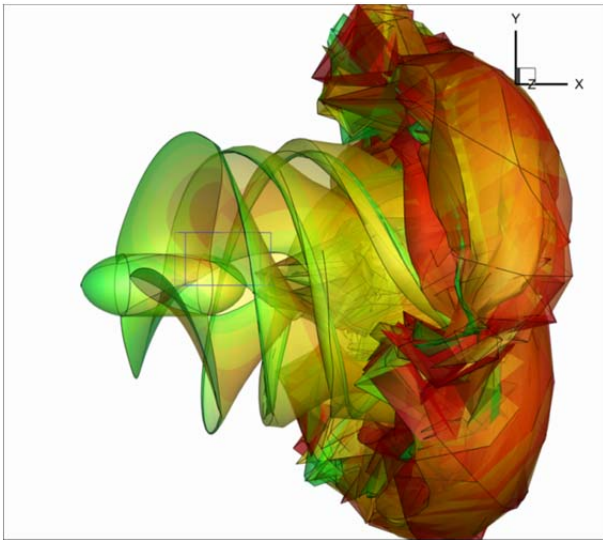
FIGURE 21. 3-D VIEW OF A FREE SHEAR LAYER AT $t = 1.0s$.
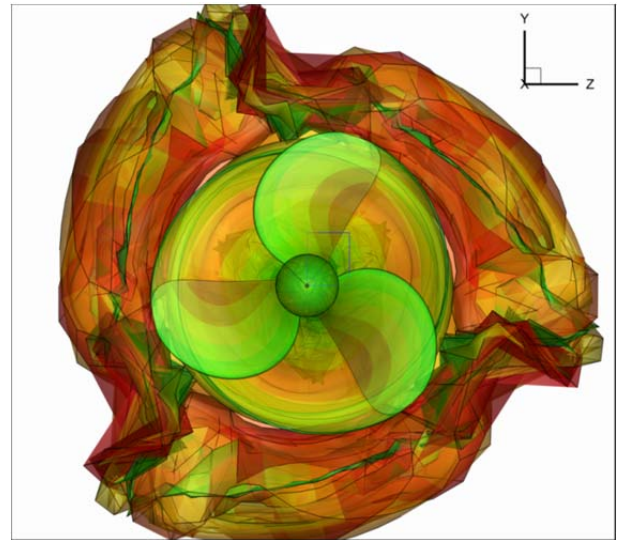$J = 0.2, R / D_{CH} = 0.05$.



FIGURE 22. YZ PROJECTED VIEW OF A FREE SHEAR LAYER
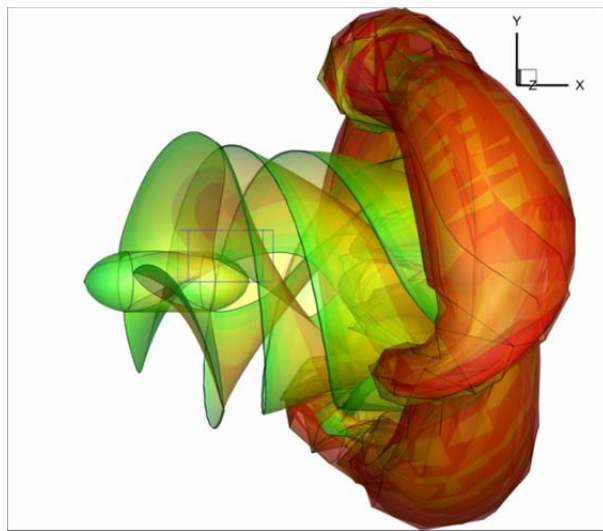AT $t = 1.0s$. $J = 0.2, R / D_{CH} = 0.05$.



FIGURE 23. 3-D VIEW OF A FREE SHEAR LAYER AT $t = 1.0s$.
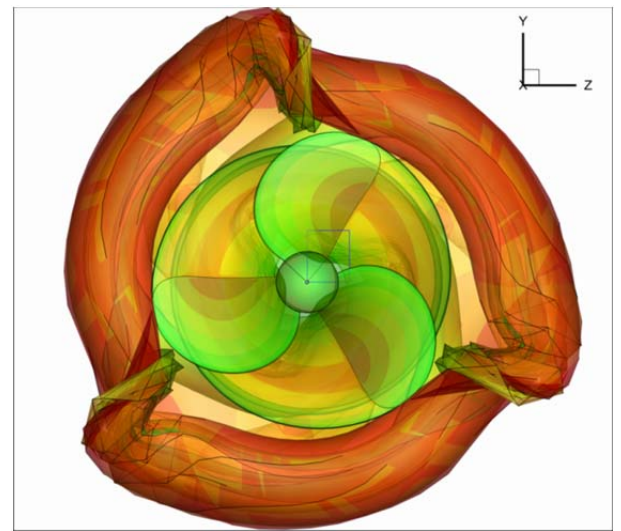$J = 0.2, R / D_{CH} = 0.1$.



FIGURE 24. YZ PROJECTED VIEW OF A FREE SHEAR LAYER
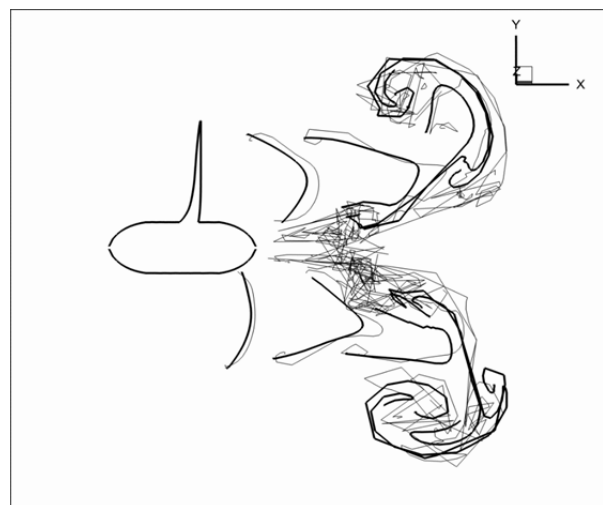AT $t = 1.0s$. $J = 0.2, R / D_{CH} = 0.1$



FIGURE 25. SLICE OF THE FREE SHEAR LAYER WITH A
PLANE CONTAINING THE Z AXIS AT $t = 1.0s$.
HAIR LINE: $R / D_{CH} = 0.05$, BOLD LINE: $R / D_{CH} = 0.1$
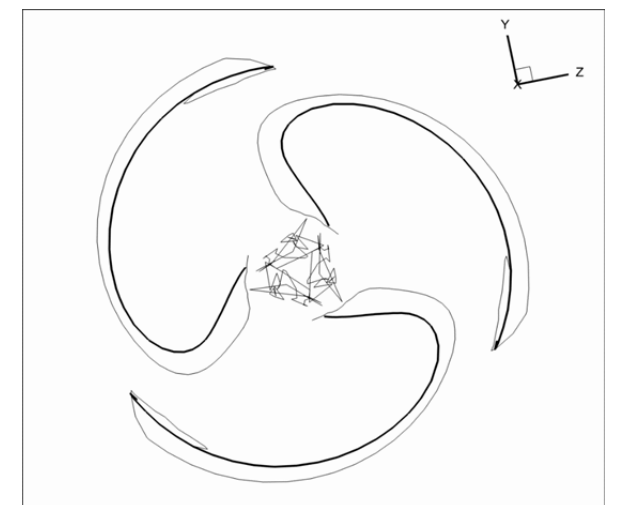


FIGURE 26. SLICE OF THE FREE SHEAR LAYER AT:
$t = 1.0s$, $x = 0.0m$ .HAIR LINE: $R / D_{CH} = 0.05$, BOLD LINE:
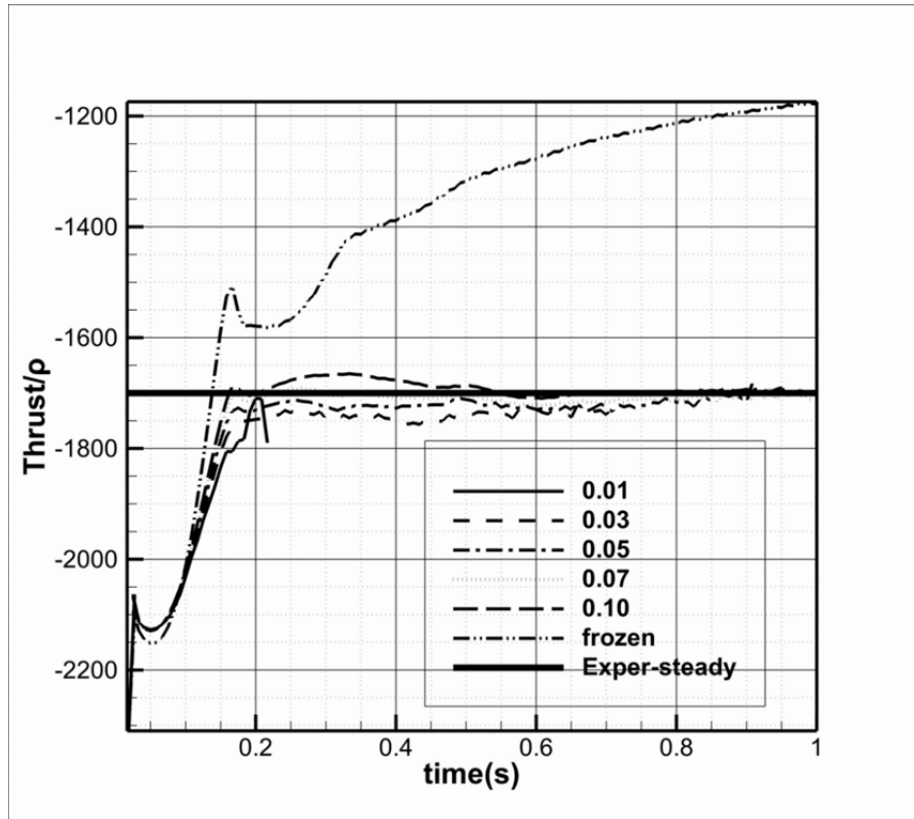$R / D_{CH} = 0.1$

FIGURE 27. PROPELLER THRUST DIVIDED BY FLUID DENSITY $\rho$ AS FUNCTION OF TIME, $J = 0.2$. PREDICTIONS WITH DIFFERENT WM'S AND COMPARISON WITH EXPERIMENTS.

*Case with $J = 0.7$*

This case is similar to the previous one in all aspects except velocity of advance which has been increased to $V = 7.98 m / s$. Again flow simulation lasts for two full propeller revolutions with a propeller angular step of 6 degrees. This results in a total simulation time of $1.0 s$ and 60 time steps per propeller turn or 120 time steps total.

Figure 28 shows the free shear layer geometry for a mollifier radius $R / D_{CH} = 0.01$. Due to the reduced loading ($J = 0.7$), instabilities in the free shear layer have been limited at the outmost (downstream) parts of it. By increasing the mollifier radius to either $R / D_{CH} = 0.05$ or $R / D_{CH} = 0.10$, the instabilities are suppressed in figures 29 and 30 respectively. From figures 28 to 30, we observe that the 'mushroom' wake pattern remains. Figures 32 and 33 compare slices of the shear layers with planes which either contain the X axis or are normal to it.

Figure 31 shows the propeller with a frozen wake model. Comparing figures 28-30 with 31 we observe that, at least near the trailing edge, the frozen wake model is a good approximation for the free wake model at this advance coefficient.

Figure 34 presents comparisons of the thrust forces obtained using either a free WM or a frozen WM with experimental results. For the free WM, the following mollifier radii have been used:

$$R / D_{CH} = 0.01, \ 0.03, \ 0.05, \ 0.07, \ 0.10$$

It is shown that the free WM results in practically the same thrust force, irrespective of the selected $R / D_{CH}$. This force is very near to the experimental measurements, Oosterveld & Oossannen (1975) [15]. On the other hand, predictions obtained using a frozen WM differ from the experimental measurements by 4% (at the end of the simulation) with a trend to increase with the passage of time in figure 34. This explains why the traditional generalized wake model used in various propeller theories (lifting line/surface theory and traditional panel methods) gives good predictions around the propeller design point.
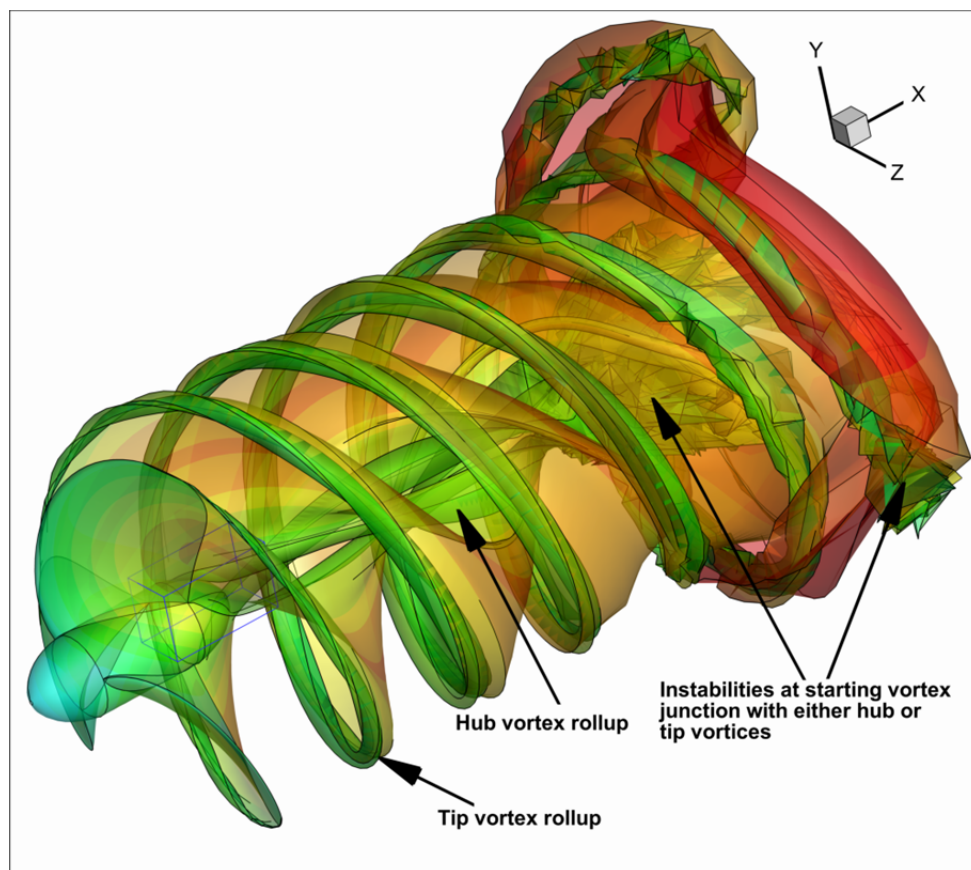
FIGURE 28. 3-D VIEW OF A FREE SHEAR LAYER AT $t = 1.0s$ . BLADES COLORED WITH POTENTIAL INTENSITY. SHEAR LAYERS COLORED WITH DIPOLE INTENSITY.   $J = 0.7, R / D_{CH} = 0.01$ .
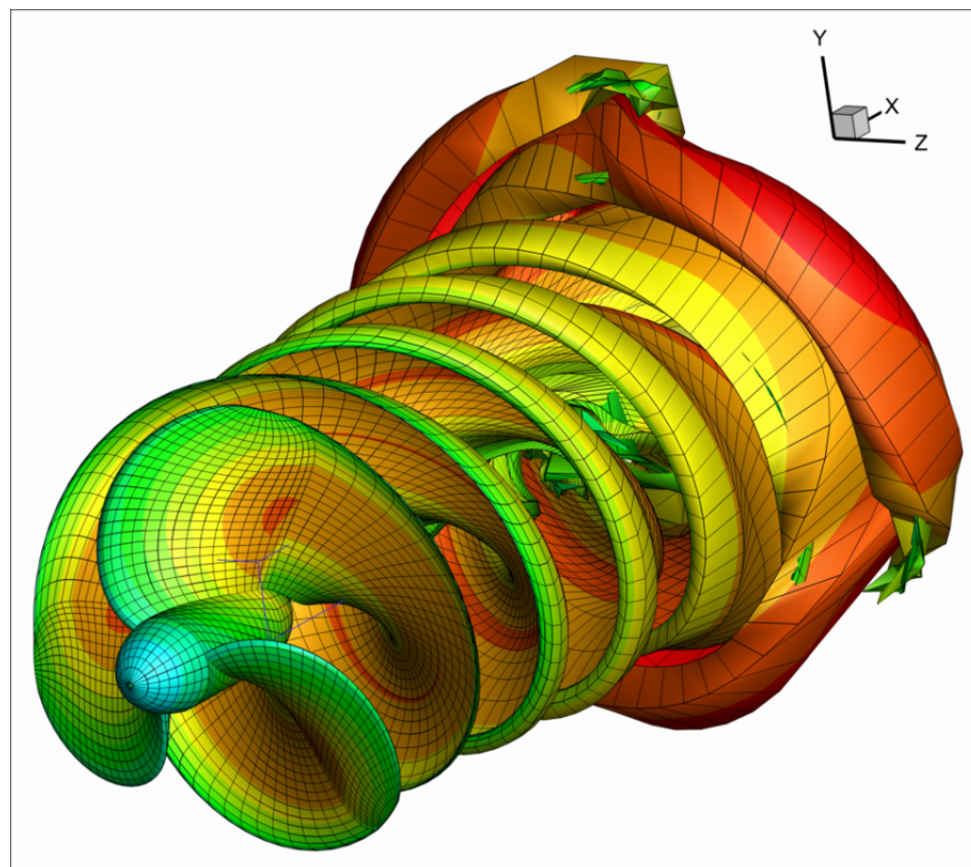


FIGURE 29. 3-D VIEW OF A FREE SHEAR LAYER AT $t = 1.0s$ .   $J = 0.7, R / D_{CH} = 0.05$ .
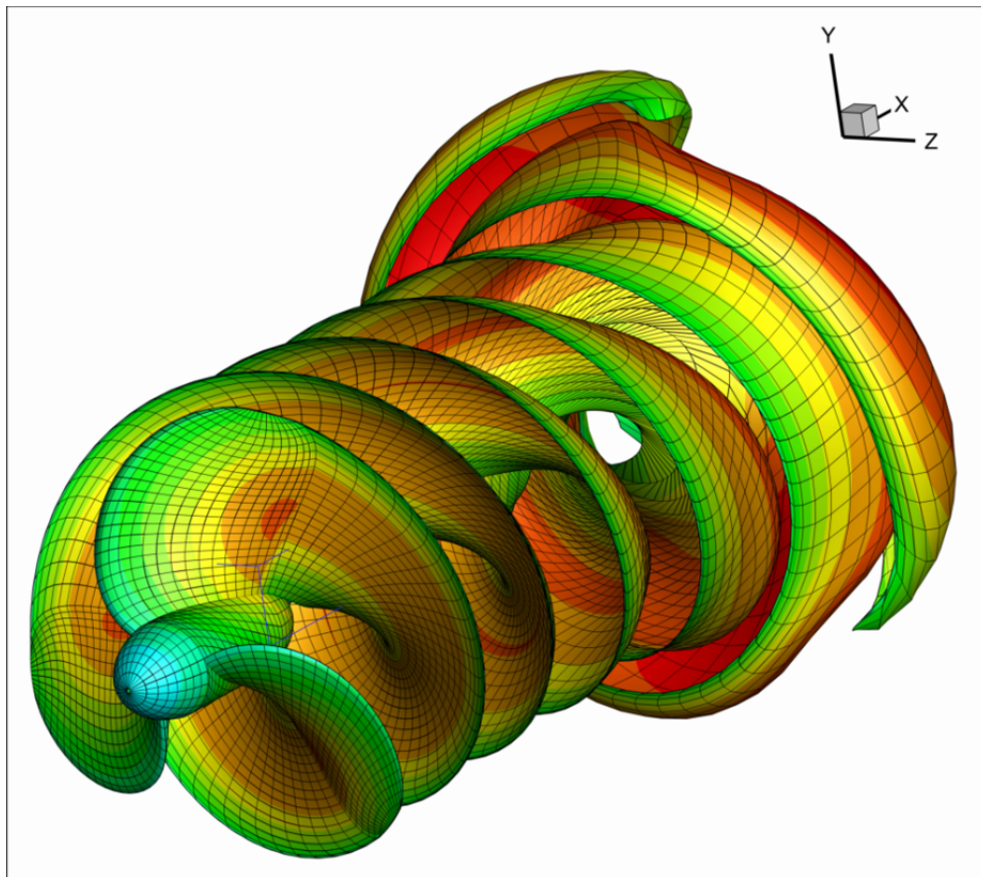
FIGURE 30. 3-D VIEW OF A FREE SHEAR LAYER AT $t = 1.0s$ . $J = 0.7, R / D_{CH} = 0.10$ .
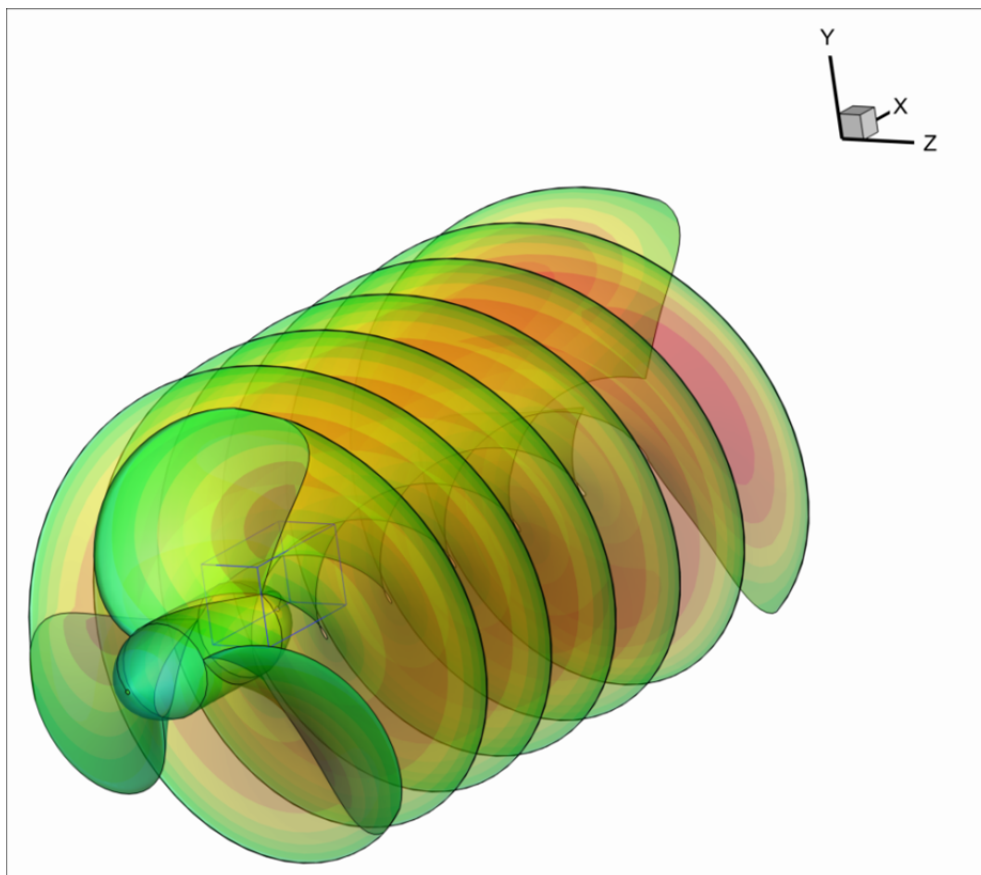


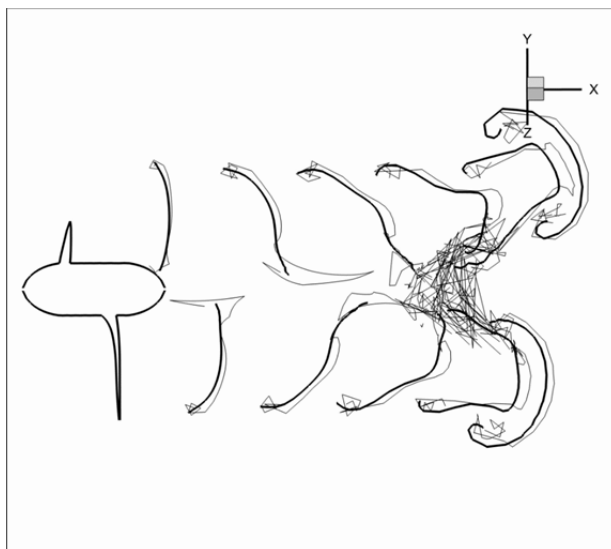FIGURE 31. 3-D VIEW OF A FROZEN WAKE MODEL AT $t = 1.0s$ , $J = 0.7$ .

FIGURE 32. SLICE OF THE FREE SHEAR LAYER WITH A PLANE CONTAINING THE Z AXIS AT $t = 1.0s$.
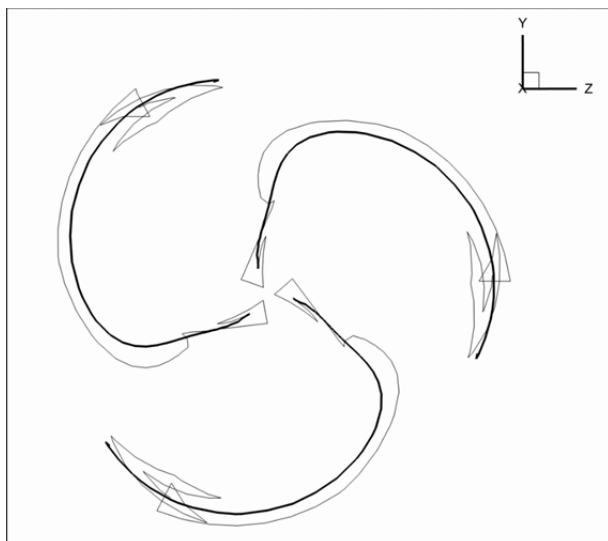HAIR LINE: $R / D_{CH} = 0.01$, BOLD LINE: $R / D_{CH} = 0.07$



FIGURE 33. SLICE OF THE FREE SHEAR LAYER AT: $t = 1.0s$, $x = -3.36m$ .HAIR LINE: $R / D_{CH} = 0.01$, BOLD LINE: $R / D_{CH} = 0.07$
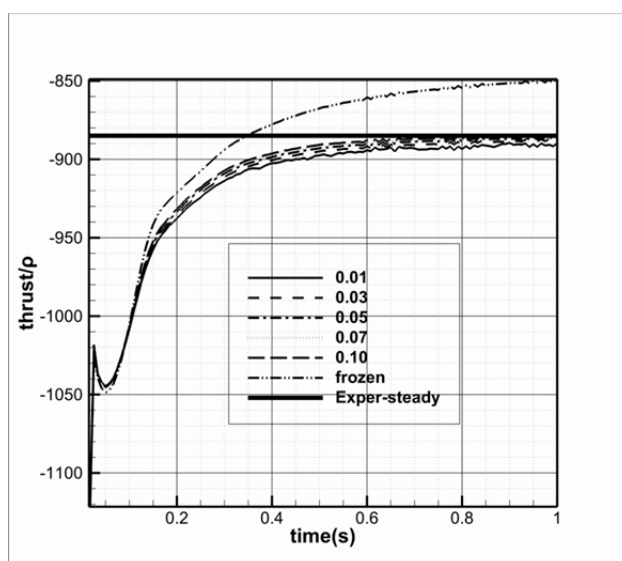


FIGURE 34. PROPELLER THRUST DIVIDED BY FLUID DENSITY $\rho$ AS FUNCTION OF TIME, $J = 0.7$ . PREDICTIONS WITH DIFFERENT
WM'S AND COMPARISON WITH EXPERIMENTS.

*The Shear Layer Geometry of a Novel Flexible Oscillating Duct Propulsor*

Our last application is the FOD (Flexible Oscillating Duct) propulsor, which conceptually has its origins in the natural paradigm of a jellyfish. Jellyfish propulsion mechanics has been investigated by Dabiri (2005, 2006) [8-9], who has made many numerical simulations and experimental investigations and has shown the feasibility of using variable diameter nozzles as propulsors. In recent years, the development of EAP (Electroactive Polymer) materials has opened the way for the construction of bulk artificial muscles, mimicking the motion of aquatic animals, Cohen ed. (2004) [5]. A characteristic property for such type of future propulsion systems is their active flexibility through an electrically controlled artificial muscle system. The FOD can be considered as a candidate EAP propulsion system, since it can produce significant thrust with good hydrodynamic efficiencies. The FOD has been introduced for the first time in Politis & Tsarsitalidis (2011) [21], where its feasibility as a ship propulsion mechanism has been presented and discussed.

The FOD is an axisymmetric duct which changes its shape with time in a specific way, determined by the motion of a section of it in a radial plane containing the FOD axis. The section of the FOD with this plane has the shape of a 2-D airfoil and its motion is similar to that of a biomimetic foil. More specifically, it performs a parallel advancement along the FOD axis superimposed to a heaving motion (normal to the axis of the FOD), a pitching motions (with angle measured from the axis of the FOD) and an oscillatory change in camber distribution, where all oscillatory motions have the same frequency, each with its own phase, Politis & Tsarsitalidis (2011) [21].

In the following example, the FOD has a diameter $D = 2m$, measured at the point of foil section pitch-axis, which is situated at 33% chord from the leading edge. The foil section has a chord $c = 1.0m$. A NACA 6412 section has been used. The FOD advances with velocity $V = 4.0m/s$. Each FOD's section performs a heave oscillation with amplitude $h_0 = 0.5m$, a pitch oscillation with amplitude $25.0\deg$ and phase $90.0\deg$ (with respect to heave) and a camber oscillation with maximum camber amplitude $m_0 = m_{6412}$ ($m_{6412}$ is the maximum camber of the NACA 6412 section) and phase $-90.0\deg$. Oscillation frequency for all motions is $2.0 rps$. BEM discretization of the FOD has been succeeded using 72 elements in the circumferential direction and 16 in the chord-wise direction (same number for face and back). Simulation lasts for two periods with 63 time steps per period or 126 time steps total. Total simulation time is $1.0s$. The Strouhal number for the FOD is $St = 0.5$. A pressure type Kutta has been used in the simulation.

Figure 35 shows the free shear layer geometry for a mollifier radius $R/D_{CH} = 0.005$ where $D_{CH} = 2m$. Extensive free vortex instabilities are observed. By increasing the mollifier radius to $R/D_{CH} = 0.10$, the instabilities are eliminated in figure 36. From the constant dipole lines which are used to color the shear layers in figures 35 and 36, we conclude that the shear-layers are composed from a set of circular ring-vortices of variable intensity, coaxial with the FOD. Furthermore, irrespective of the filter used, the free shear layers occupy a certain region of the 3-D space with a well-recognized pattern. This pattern resembles the shape of a row of 'flying saucers' (one per period) with diameters proportional to their age (i.e. older 'flying saucers' have greater diameters).

Figure 37 presents comparisons of the FOD thrust force obtained using either a free WM or a frozen WM. For the free WM, the following mollifier radii have been used:

$$R/D_{CH} = 0.005,\ 0.01,\ 0.05,\ 0.10$$

Regarding predicted thrust force using the free WM, we observe that with the exception of the time neighborhoods of $t = 0.26s$ and $t = 0.76s$, the results are almost independent of the mollifier radius as in all previous examples. For the time neighborhoods around $t = 0.26s$ and $t = 0.76s$, which coincide with the points where thrust is maximized (in absolute value), mollifier independent thrust is obtained only for mollifier radii less than 0.01. Curiously enough, around the third point $t = 0.54s$, where thrust is maximized, the calculated thrust is nearly independent from the mollifier radius in the whole range of its variation in figure 37. To understand the cause of this behavior we concentrate at the structure of the free wake vorticity and more specifically to its relative position with the FOD, at points where thrust is maximized. The structure of the free wake vorticity at $t = 0.54s$ and $t = 0.76s$ for $R/D_{CH} = 0.10$ is shown in figures 38 and 39 respectively. From figure 38, it is shown that at $t = 0.54s$ the thrust-maximum occurs during the FOD expansion phase, while at $t = 0.76s$ the thrust-maximum occurs during the FOD contraction phase. Furthermore, the corresponding free wake positions, with respect to the FOD, are entirely

different for the two cases; it is a fact which explains why the value of the mollifier radius affects differently the calculated thrust.

More specifically, during the expansion phase, the stronger wake ring vortices are relatively far from the FOD section. As a result, the calculated thrust is independent from the mollifier radius in the whole range of its variation. During the FOD contraction phase, the stronger wake ring-vortices are closer to the FOD section trailing edge. This has a pronounced effect on the Kutta condition and consequently to the calculated FOD pressures and forces. The effect of the mollifier radius to the position of the free shear layer at $t = 0.76s$ is shown in figure 40, where hair lines denote the free shear layer geometry for $R/D_{CH} = 0.005$ while bold lines denote free shear layer geometry for $R/D_{CH} = 0.10$. From this figure, we observe that the mollifier radius affects the position of the shear layer in the vicinity of the FOD trailing edge, explaining thus the dependence of thrust from the mollifier radii at $t = 0.76s$ as shown in figure 37.

Finally notice that in the case of a FOD, thrust predictions obtained using a frozen WM differ considerably from that with a free WM in figure 37.
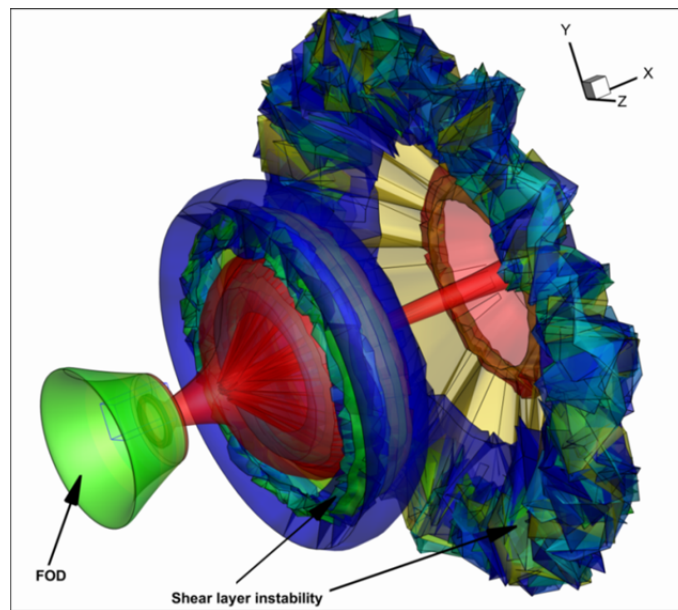


FIGURE 35. FREE SHEAR LAYER OF A FOD AT $t = 1.0s$. EXTENSIVE SHEAR LAYER INSTABILITIES OCCUR. FOD COLORED WITH POTENTIAL INTENSITY. SHEAR LAYER COLORED WITH DIPOLE INTENSITY. $St = 0.5, R/D_{CH} = 0.005$
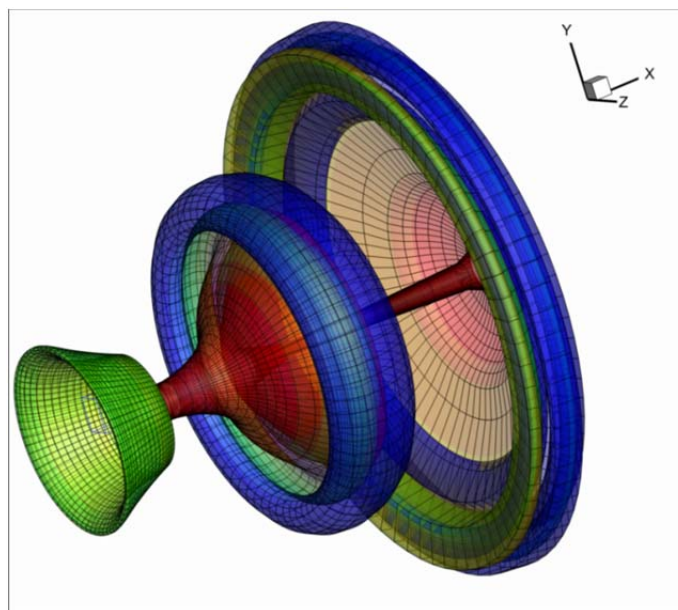


FIGURE 36. FREE SHEAR LAYER OF A FOD AT $t = 1.0s$. VORTEX INSTABILITIES HAVE BEEN SUPPRESSED. $St = 0.5, R/D_{CH} = 0.10$
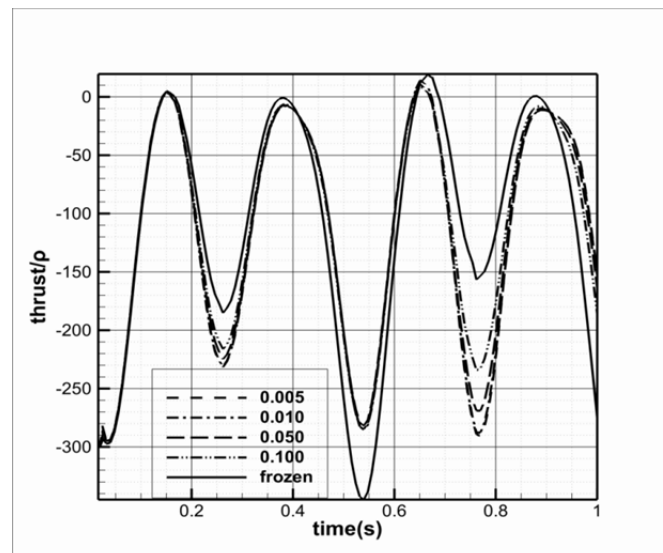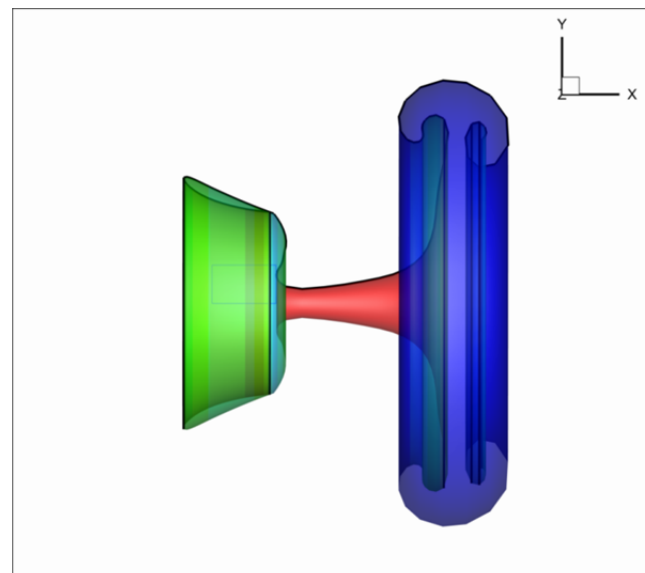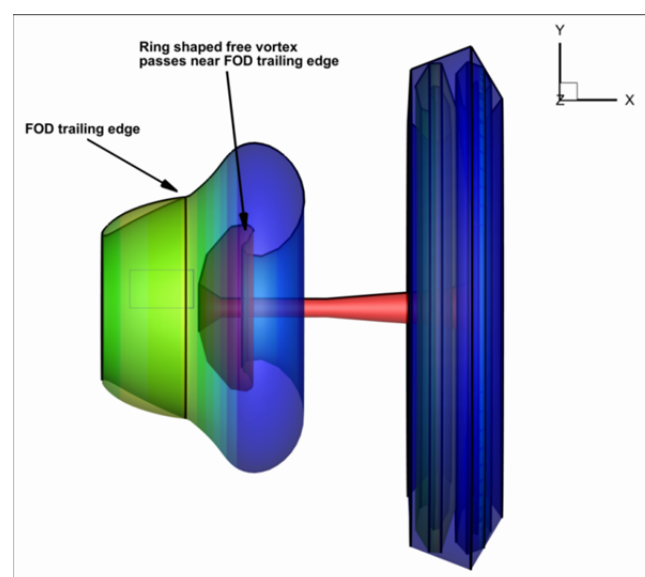
FIGURE 37. THRUST (X-AXIS) FORCE OF THE FOD – PREDICTIONS WITH DIFFERENT WAKE MODELS.



FIGURE 38. FREE SHEAR LAYER OF A FOD AT $t = 0.54s$ . $R/D_{CH} = 0.10$



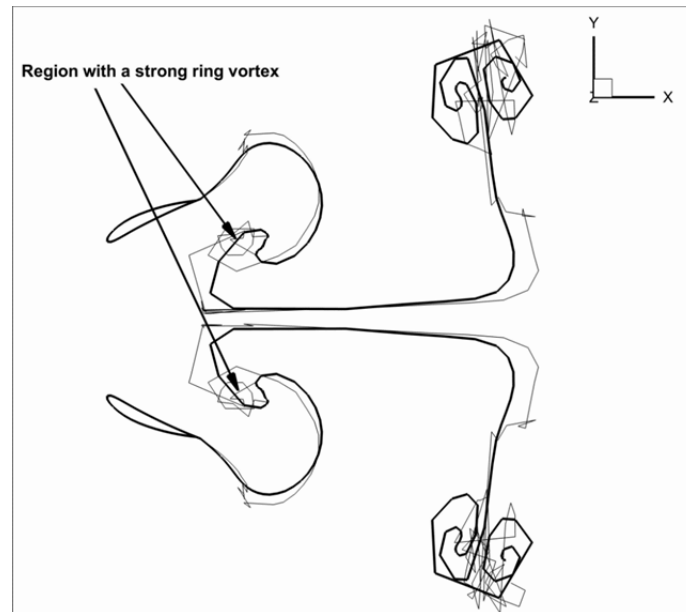FIGURE 39. FREE SHEAR LAYER OF A FOD AT $t = 0.76s$ . $R/D_{CH} = 0.10$

FIGURE 40. SLICE OF THE FREE SHEAR LAYER DURING FOD CONTRACTION ( $t = 0.76s, z = 0.0m$ )

HAIR LINE: $R / D_{CH} = 0.005$ , BOLD LINE: $R / D_{CH} = 0.10$

## Conclusions

The details of a filtering technique are presented, which in combination with a boundary element formulation and a time stepping algorithm can be used to simulate the motion of the free shear layers, produced in cases of incompressible non-viscous flows around systems of unsteadily moving rigid or flexible lifting bodies. This is a major innovation in treating complex unsteady propulsion problems since no simplifying assumptions (like that of a frozen or generalized wake) are necessary. The method has been applied to a number of flows around lift producing configurations, performing unsteady motions with practical interest. From the systematic calculations, the following conclusions can be drawn:

In all cases, there is a certain non-dimensional range for the mollifier radius, almost problem independent, where the free wake vorticity is trapped inside a subset of the 3-D space and forms a well-recognized pattern. For the simulated cases, this 'attracting configuration' varies considerably from case to case. More specifically: (a) for a steadily moving wing it is a quadrilateral ring-vortex with roll-up at its free edges (tip vortices and starting vortex), (b) in the case of a biomimetic wing it is a repeated S-shaped pattern of oblique ring vortices or equivalently a reverse Karman Vortex Street, (c) in the case of a burst starting propeller it is a 'mushroom' type 3-D vortex pattern, while (d) in the case of a FOD it has the shape of a row of 'flying saucers' with increasing diameters, the number of which is equal to the number of the simulation periods.

For smaller values of the mollifier, radius instabilities or even chaotic behavior are almost always present in the distribution of the free vorticity inside the attracting configuration. By increasing the mollifier radii or using age dependent mollifier radii, those instabilities gradually disappear. It is of great importance that chaotic distributions of the wake vorticity, obtained for the lower mollifier radii, result in predictions for forces very close to each other, as far as the vorticity remains inside its attracting configuration and it is not so close to the body boundaries. This result indicates that under the seemingly chaotic picture in the free shear layer vortices, some type of order still exists.

From the simulations, it is shown that in the range of the Strouhal numbers where natural flyers and swimmers operate, the frozen wake model can be an attractive alternative for preliminary force predictions.

**REFERENCES**

[1]  Andro, J.Y & Jacquin, L. (2009). 'Frequency effects on the aerodynamic mechanisms of a heaving airfoil in a forward flight configuration'. Aerospace Science and Technology, 13: 71–80.

[2]   Bajer, K. & Moffatt, H.K. (2004). 'Tubes, Sheets and Singularities in Fluid Dynamics'. Kluwer Academic, New York.

[3]   Borazjani, I. & Sotiropoulos, F. (2008). 'Numerical investigation of the hydrodynamics of carangiform swimming in the transitional and inertial flow regimes'. J. of Experimental Biology, 211: 1541-1558.

[4]   Bohl, D.G. & Koochesfahani, M.M. (2009). 'MTV measurements of the vortical field in the wake of an airfoil oscillating at high reduced frequency'.  J. Fluid Mechanics, 620: 63–88

[5]   Cohen, Y.B. ed. (2004). 'Electroactive Polymer (EAP) Actuators as Artificial Muscles – Reality, Potential, and Challenges'. SPIE Press.

[6]   Dabiri, J.O. & Gharib, M. (2005a). 'Starting flow through nozzles with temporally variable exit diameter'. J. of Fluid Mechanics, 538: 111–36.

[7]   Dabiri, J.O. & Gharib, M. (2005b). 'The role of optimal vortex formation in biological fluid transport'. Proc. R. Soc., B 272: 1557–60.

[8]   Dabiri, J.O., Colin, S.P. & Costello, J.H. (2006). 'Fast-swimming hydromedusae exploit velar kinematics to form an optimal vortex wake'. J. Exp. Biol., 209:2025–33

[9]   Dong, H., Mittal, R. & Najjar, F.M. (2006). 'Wake topology and hydrodynamic performance of low-aspect-ratio flapping foils'. J. of Fluid Mechanics, 566: 309–43

[10]  Katz, J. & Plotkin, A. (2001). 'Low speed aerodynamics - From wing theory to panel methods'. Cambridge aerospace series. Cambridge University Press.

[11]  Krasny, R., Lindsay, K. & Nitsche, M. (2002). 'Simulation of vortex sheet roll-up: chaos, azimuthal waves, ring merger'. In: Bajer, K. & Moffatt, H.K. eds. 'Tubes, Sheets and Singularities in Fluid Dynamics'. Kluwer Academic, New York.

[12]  Marchioro, C. & Pulvirenti, M. (1994). 'Mathematical Theory of Incompressible Nonviscous Fluids'. Springer-Verlag.

[13]  Mikhlin, S.G. (1965), 'Multidimensional singular integrals and integral equations'. Pergamon press.

[14]  Muijres, F.T. & Lentink, D. (2007). 'Wake visualization of a heaving and pitching foil in a soap film'. Exp Fluids 43: 665–673.

[15]  Oosterveld, M.W.C. &  Oossannen, P. (1975). 'Further Computer Analyzed Data of the Wagenigen B-Screw Series'. International Shipbuilding Progress, vol. 22.

[16]  Parker, K., von Ellenrieder, K. D. & Soria, J. (2007). 'Morphology of the forced oscillatory flow past a finite-span wing at low Reynolds number'. J. of Fluid Mechanics, 571: 327–357.

[17]  Parker, K., von Ellenrieder, K. D. & Soria, J. (2008). 'Fluid mechanics of flapping wings'. Experimental Thermal and Fluid Science 32: 1578–1589.

[18]  Politis G.K. (2004). 'Simulation of Unsteady motion of a Propeller in a fluid including Free Wake Modeling'. Journal of Engineering Analysis with Boundary Elements, 28(6): 633-653.

[19]  Politis G.K. (2009).'A BEM code for the calculation of flow around systems of independently moving bodies including free shear layer dynamics'. Advances in Boundary Element Techniques X.

[20]  Politis, G.K. (2011). 'Application of a BEM time stepping algorithm in understanding complex unsteady propulsion hydrodynamic phenomena'. Ocean Engineering, 38: 699-711.

[21]  Politis, G.K. & Tsarsitalidis, V. (2011). 'Exploring the Potential of an Oscillating Duct as a Marine Propulsor'. Second International Symposium on Marine Propulsors, smp'11, Hamburg, Germany.

[22]  Ramsey, W.D. (1996). 'Boundary Integral Methods for lifting Bodies with Vortex Wakes'. PhD thesis, MIT Department of Ocean Engineering.

[23]  Riley, A.J. & Lowson, M.V. (1998). 'Development of a three-dimensional free shear layer'. J. Fluid Mech. 369:49-89.

[24]  Rozhdestvensky, K.V. & Ryzhov, V.A. (2003). 'Aerohydrodynamics of flapping-wing propulsors'. Progress in aerospace sciences, 39: 585-633.

[25]  Saffman, P.G. (1992). 'Vortex Dynamics'. Cambridge University press.

[26]  Sarpkaya, T. (1989). 'Computational methods with vortices – The 1988 Freeman Scholar Lecture'. Journal of Fluids Engineering, Vol. 111/5.

[27] Shyy, W., Lian, Y., Tang, J., Viieru, D. & Liu, H. (2008). 'Aerodynamics of Low Reynolds Number Flyers'. Cambridge Aerospace Series, ISBN-13 978-0-511-47871-0.

[28] Stettler, J.W. (2004). 'Steady and Unsteady Dynamics of an Azimuthing Podded Propulsor Related to Vehicle Maneuvering'. PhD thesis, MIT.

[29] Taylor, G. K., Nudds, R. L., & Thomas, A. L. R. (2003). 'Flying and swimming animals cruise at a Strouhal number tuned for high power efficiency'. Nature (London) 425, 707–11.

[30] Taylor, G.K., Triantafyllou, M.S. & Tropea, C. (eds.). (2010). 'Animal Locomotion'. Springer-Verlag Berlin Heidelberg, ISBN 978-3-642-11632-2.

[31] Triantafyllou, M. S., Triantafyllou, G. S., & Yue, D. K. P. (2000). 'Hydrodynamics of fishlike swimming'. Annual Review of Fluid Mechanics 32, 33–53.

[32] Wang, Z., Chen, P. & Zhang, X. (2008). 'Wake Vortex Structure Characteristics of a Flexible Oscillating Fin'. Journal of Bionic Engineering, 5: 49−54.

[33] Winckelmans, G.S. & Leonard, A. (1993). 'Contributions to Vortex Particle Methods for the Computation of Three-Dimensional Incompressible Unsteady Flows'. J. of Computational Physics, 109:247-273.

[34] Wood, T.H. & Grace S.M. (2000). 'Free Wake Analysis for Calculating the Aeroacoustics of a Wing-Flap Configuration'. 38th AIAA Aerospace Sciences Meeting, paper AIAA 2000–0607.

[35] Wu, J.Z., Ma, H.Y. & Zhou, M.D. (2006). 'Vorticity and Vortex Dynamics'. Springer-Verlag Berlin Heidelberg.

[36] Zhang, N. & Zheng, Z.C. (2009). 'Flow/pressure characteristics for flow over two tandem swimming fish'. Computers & Fluids, 38: 1059–1064.